The Astrophysical Journal, 904:87 (22pp), 2020 December 1 https://doi.org/10.3847/1538-4357/abbf54

Hinode/EIS Measurements of Active-region Magnetic Fields

E. Landi[1], R. Hutton[2], T. Brage[3], and W. Li[3,4]
[1] Department of Climate and Space Sciences and Engineering, University of Michigan, USA; elandi@umich.edu
[2] Institute of Modern Physics, Fudan University, Shanghai 200433, People's Republic of China
[3] Department of Physics, Lund University, Box 118, SE-22100 Lund, Sweden
[4] Department of Materials Science and Applied Mathematics, Malmö University, SE-20506, Malmö, Sweden
Received 2020 July 10; revised 2020 October 6; accepted 2020 October 6; published 2020 November 24

Abstract

The present work illustrates the potential of a new diagnostic technique that allows the measurement of the coronal magnetic field strength in solar active regions by utilizing a handful of bright Fe X and Fe XI lines commonly observed by the high-resolution Hinode/EUV Imaging Spectrometer (EIS). The importance of this new diagnostic technique is twofold: (1) the coronal magnetic field is probably the most important quantity in coronal physics, being at the heart of the processes regulating space weather and the properties of the solar corona, and (2) this technique can be applied to the existing EIS archive spanning from 2007 to 2020, including more than one full solar cycle and covering a large number of active regions, flares, and even coronal mass ejections. This new diagnostic technique opens the door to a whole new field of studies, complementing the magnetic field measurements from the upcoming DKIST and UCoMP ground-based observatories, and extending our reach to active regions observed on the disk and until now only sampled by radio measurements. In this work, we present a few examples of the application of this technique to EIS observations taken at different times during the EIS mission, and we discuss its current limitations and the steps to improve its accuracy. We also present a list of EIS observing sequences whose data include all of the lines necessary for the application of this diagnostic technique, to help the solar community navigate the immense set of EIS data and to find observations suitable for measuring the coronal magnetic field.

Unified Astronomy Thesaurus concepts: Solar magnetic fields (1503); Solar corona (1483)

1. Introduction

The magnetic field of the solar corona is one of the most critical parameters in solar physics, as it lies at the core of most manifestations of coronal physics and of the interactions between the Sun and its planetary system. In fact, the magnetic field confines and structures coronal plasmas at all temperature and spatial scales, from bright points (a few tens of arcseconds in size) to coronal loops and active regions (arcminutes) and streamers (solar radii). Also, regions of open and closed magnetic fields have very different properties, with the former being the site of the acceleration of the fast solar wind and possibly of a part of the slow solar wind (Stakhiv et al. 2015, 2016). Several types of magnetic waves have been proposed as candidates to heat the solar coronal plasmas up to multimillion degree temperatures, as well as to accelerate the solar wind along open magnetic field lines (e.g., Cranmer 2009; Gombosi et al. 2018 and references therein). Magnetic reconnection has been suggested as a viable alternative for coronal heating and wind acceleration (Cranmer 2009), and it is thought to be the trigger of both flares and coronal mass ejections (Webb & Howard 2012 and references therein).

Despite its importance, the coronal magnetic field has proved elusive to infer directly, and very few measurements have been carried out. The photospheric magnetic field has been routinely measured by a number of space missions in the last few decades by instruments such as SoHO/MDI (Scherrer et al. 1995), Hinode/SOT (Suematsu et al. 2008), and SDO/HMI (Scherrer et al. 2012), and it is a fundamental component of local and global models of the solar atmosphere. Measurements of the coronal magnetic field are more difficult, because of the weakness of its signatures and of the complexity of the measurements. Indirect measurements have been carried out using coronal loop seismology (de Moortel et al. 2016) and, recently, long-duration observations of waves in the solar corona from the Coronal Magnetometer and Polarimeter (CoMP; Tomczyk et al. 2008), the latter providing maps of the plane-of-the-sky component of the coronal magnetic field at the limb (Yang et al. 2020). Note that CoMP measurements cannot provide information on the magnetic field on the disk. The magnetic field morphology has been empirically derived from the active-region plasma distribution from both visible and EUV observations. The only direct measurements so far have been obtained with radio observations and spectro-polarimetry of visible and near-infrared (NIR) radiation, mostly with CoMP.

To improve on CoMP measurements, and to provide at the same time measurements both of the magnetic field and of coronal plasma properties, two new ground-based facilities are being built and are becoming operational in 2020: the Upgraded CoMP (UCoMP; S. Tomczyk et al. 2020, in preparation), and most importantly the Daniel K. Inouye Solar Telescope (DKIST). Both facilities will measure the coronal magnetic field through visible and NIR spectropolarimetry, with vastly different fields of view and resolution: while the DKIST observatory (which will comprise a host of different instruments) will provide high-spatial-resolution measurements over a small field of view, UCoMP will provide near-simultaneous lower resolution measurements over the entire solar corona.

However, ground-based spectropolarimetric magnetic field measurements of the coronal magnetic fields suffer from a few fundamental limitations. First, they are affected by the day/night cycle and by atmospheric transmission and scattering, although such a limitation has been overcome by space-based

instruments. Second, since they observe in the visible and NIR wavelength ranges, they can only carry out measurements at the limb using coronographs, as the photospheric brightness prevents any measurements of coronal emission from being carried out on the disk. Third, limb observations in the visible and NIR can only provide the magnetic field orientation in the plane of the sky (through linear polarization: Stokes U and Q) and the magnetic field component along the line of sight (through circular polarization: Stokes V), so the total magnitude of the magnetic field cannot be reconstructed. Furthermore, the signal of Stokes V is weaker than the signal of Stokes U and Q, so often only the magnetic field orientation in the plane of the sky can be measured.

The only measurements of coronal magnetic fields on the disk are done using radio measurements, sometimes in combination with EUV observations. These measurements, however, are typically able to yield magnetic field strengths usually in excess of ≈200 G and thus are most suitable for active regions. For example, Brosius et al. (2002) and Brosius & White (2006) combined EUV and radio observations of active regions on the disk to infer magnetic field strengths in the 580–1750 G range. White et al. (2002) measured the magnetic field of a flaring loop and found that it ranged from ≈800 G at the footpoints to 224 G at the top; similar values were found by Nindos et al. (2000, 870 G to 280 G). Still, radio measurements are able to provide the magnetic field at different heights within the same magnetic structure, but are not able to determine the actual height of the structure itself, thus leaving a signficant uncertainty on the 3D orientation of the magnetic field vector.

Disk observations of the solar corona have been routinely carried out by imaging instruments and high-resolution spectrometers observing in the X-ray, EUV, and ultraviolet wavelength ranges by a host of rocket flights and space missions (e.g., del Zanna & Mason 2018 and references therein). These instruments constitute the backbone of our studies of the solar corona, as these wavelength ranges include a wealth of spectral lines and continuum radiation that provide plasma diagnostic tools allowing us to measure fundamental plasma properties such as electron densities and temperatures, plasma motions, and elemental composition (Phillips et al. 2008; del Zanna & Mason 2018). However, the effects of coronal magnetic fields on the intensities, wavelengths, and profiles of emission lines in the X-ray, EUV, and UV ranges are too small to be detected, so no diagnostic tool is available to measure the magnetic field directly from line intensities in these wavelength ranges.

Recently, Li et al. (2015, 2016) and Si et al. (2020b) reported on a peculiar atomic physics configuration that makes the wave function composition of a low-energy metastable atomic level of Fe X sensitive to the presence of an external magnetic field. This sensitivity would remain a curious feature of a single, metastable Fe X if this level did not happen to significantly contribute to the emission of one of the strongest lines in the Fe X spectrum in the solar corona at 257.26 Å. The properties of this metastable level cause the intensity of the line it emits to be directly and significantly affected by the local magnetic field strength; since this ion is usually formed in the corona, this property opens a window through which we can directly measure the magnetic field strength in the solar corona, which was first explored by Si et al. (2020a).

The 257.26 Å line has been routinely observed by the EUV Imaging Spectrometer (EIS; Culhane et al. 2007) on board the Hinode satellite (Kosugi et al. 2007), along with many other Fe X lines for more than one solar cycle (2007 to mid-2020 at the time of writing). The vast data set accumulated by the EIS mission can be utilized to measure the coronal magnetic field strengths throughout the solar cycle. The first application of this line to determine magnetic fields in a Hinode/EIS active region has been described by Si et al. (2020a).

The goal of this paper is to refine and extend the diagnostic technique by making use of a few of the strongest Fe X and Fe XI lines routinely observed by the Hinode/EIS spectrometer from 2007 to 2020 to measure the magnetic field of the solar corona, present some examples, and discuss this diagnostic technique's strengths and limitations, as well as its synergies with the upcoming DKIST and UCoMP observatories. Future papers will apply this diagnostic technique to a number of different open problems in the solar corona. Section 2 introduces the diagnostic technique and its physical bases, Section 3 describes the Hinode/EIS observing sequences that can be used to apply the technique, as well as the actual observations we analyzed, and Section 4 presents the magnetic field measurements we obtained. Section 5 discusses the uncertainties in the present method, and Section 6 suggests future steps to improve on this technique.

2. Methodology

2.1. History of Magnetically Induced Transitions

The influence of magnetic fields on atomic energy levels has a history going back to Zeeman in 1896. The Zeeman effect is used in many areas to measure the strength of external magnetic fields. What is much less known is the influence of external magnetic fields on the lifetimes of long-lived levels, through an introduction of a new decay channel, potentially resulting in new spectral features. The idea that a magnetic field could shorten the lifetime of a long-lived level was investigated in the 1960s and was labeled *Zeeman quenching* by Feldman et al. (1967). The quenching was only considered through the shortening of, for example, the $1s2s2p\ ^4P_{5/2}$ lifetime in Li I and as an error source when trying to estimate the lifetimes in an expected field-free space. The idea of a new or a change in an existing feature due to an external field did not seem to have any practical applications, and the studies did not flourish. More recently, Beiersdorfer et al. (2003) used the Electron Beam Ion Trap (EBIT) at the Lawrence Livermore National Laboratory for the first observation of a spectral line induced by an external magnetic field: the $2p^5\ 3s\ ^3P_0$–$2p^6\ ^1S_0$ transition in Ne-like argon. This transition is strictly forbidden (being $J = 0$ to $J = 0$) in the absence of an external magnetic field (or nuclear spin). The induction of this transition requires a field of a few tesla and was considered mainly important for understanding the atomic structure (as well as predicting nuclear properties in nonzero spin isotopes), not for applications to astrophysical plasmas: the required field and low density did not offer any possible observations.

Some years later, a study was initiated by some of the present authors (T.B., R.H., W.L.) to find transitions induced by much lower magnetic field strengths. The basic atomic structure needed for the induction of a spectral line through an external magnetic field is two energy levels relatively close in energy, where one has an allowed decay, and therefore short

lifetime, while the other one should be at least metastable with a considerably longer lifetime. If the effect should be observable for small magnetic fields, the energy splitting between the levels has to be small, so the search focused on "accidental" pseudodegeneracy, induced by level crossing in the gross structure of ions, along an isoelectronic sequence. It represented a major breakthrough when the project focused on the interesting isoelectronic behavior of the $3\,s^2\ 3p^4\ 3d\ ^4D$ term in Cl-like ions, observed by isoelectronic studies and observations as reported in the NIST database (Kramida et al. 2019).

The ^4D term has four energy levels, of which the $^4D_{7/2}$ level is metastable and can only decay to the ground $J = 3/2$ level of the $3s^2\ 3p^5\ ^2P$ term by a forbidden magnetic quadrupole (M2), in the absence of an external field, because J must change by two units. However, the $^4D_{5/2}$ level has an allowed electric dipole (E1) decay channel to the $^2P_{3/2}$ level (albeit spin-changing), leading to a lifetime that is five orders of magnitude shorter. The ordering of these two levels changes along the sequence, and as discussed by Li et al. (2015), the minimum energy separation between these two levels occurs for Fe X, leading to a pseudodegeneracy. In this work, it was shown for the first time that there was definitely a magnetic-induced transition (MIT) from the $^4D_{7/2}$ level of Fe X, induced by the external magnetic field mixing of the two levels: the $J = 7/2$ level acquires some of the $J = 5/2$ level's properties, including a decay channel to the ground term. It was also clear that this MIT was sensitive to fairly small magnetic fields. One problem discussed by Li et al. (2015) was the fact that the energy splitting of the two levels, which is crucial for the required sensitivity of the MIT to the low-enough external magnetic field strengths, was not known accurately enough. In a subsequent work by Li et al. (2016), the Shanghai high-temperature superconducting EBIT with known magnetic field was used to obtain a value for the $^4D_{5/2}$-$^4D_{7/2}$ fine structure energy. The energy obtained was 3.5 cm^{-1}, which agreed with the astrophysical estimate of 0–5 cm^{-1}, but with a large uncertainty (the astrophysical estimate does not offer any explicit guidance on uncertainty). Li et al. (2016) also showed that a line ratio of the $^4D_{7/2}$ and $^4D_{5/2}$ transitions blended with the transition from one of the other ^4D levels could be used as a magnetic field diagnostic. Inspired by these initial efforts, Judge et al. (2016) used spectra of the solar corona from SkyLab to improve on the uncertainty of the $^4D_{5/2,7/2}$ fine structure energy and arrived at the result of $3.6 \pm 2.7\ \mathrm{cm}^{-1}$. Recently, this fine structure value was used in a determination of the magnetic field for an active region of the solar corona from spectral data from Hinode (Si et al. 2020a). Even more recently, Landi et al. (2020) improved on the measurement by Judge et al. (2016) using spectra from the SOHO/SUMER high-resolution spectrometer, to obtain an energy separation of $2.29 \pm 0.50\ \mathrm{cm}^{-1}$, which significantly lowered the uncertainty (see Section 5); in the present work, we will be using this value.

2.2. Conceptual Description of the MIT

The core of the method discussed in this paper is the concept of mixing of atomic states of the same parity but different J-values. The strength of the mixing depends strongly on the separation of the levels in energy and the magnetic field strength (both squared). All interactions between the electrons are diagonal in the total angular momentum quantum number J. Therefore, two levels such as the $3\,s^2\ 3p^4\ 3d\ ^4D_{5/2}$ and $^4D_{7/2}$ in Cl-like ions cannot be mixed due to electron–electron interaction, even if the levels are basically energy degenerate. To induce this mixing and thereby the decay of the metastable level, we need to introduce interactions outside the electronic cloud, such as an externally applied magnetic field, which can mix levels with J differing by 0 or ± 1. The other possibility for this mixing to occur is through a nuclear spin, which changes the total angular momentum of the ion. In the cases reported here, we only consider nuclei with zero spin.

It is important to note that the mixing of the $3s^2\ 3p^4\ 3d\ ^4D_{5/2}$ and $^4D_{7/2}$ and the resulting MIT in Cl-like Fe can be induced by unexpectedly small fields, on the order of a few hundred gauss (or less). This is to be compared to the internal magnetic field of Fe X, caused by the orbiting electrons and their spins, which is of the order of many hundreds or even thousands of tesla. As a metaphor, one could say that the external field only tickles the ion, but the accidental pseudodegeneracy of two levels causes it to decay with an EUV photon from the metastable state.

2.3. Measuring the Magnetic Field with the MIT

In principle, any Fe X line intensity ratio involving 257.26 Å is dependent on the magnetic field. However, two important features need to be considered:

1. The upper $^4D_{7/2}$ level is metastable, so all ratios involving the M2 and MIT lines are density sensitive.
2. The EIS 257.26 Å is an unresolved blend of the E1, M2, and MIT transitions.

The first property makes it imperative to carry out an independent measurement of the electron density before determining the magnetic field.

The second property is due to the energy separation between the $^4D_{7/2}$ and $^4D_{5/2}$ levels giving rise to an ≈4 mÅ wavelength difference between the E1 and the (MIT+M2) transitions, which is by far too small to be resolved by any high-resolution spectrometer built so far and is also much smaller than the line broadening in the corona. Thus, the MIT and M2 individual intensities need to be determined by indirect means.

Furthermore, at low densities the E1 and M2 transitions are predicted to have similar intensities, while at high densities the E1 transition dominates the blend as collisions with free electrons depopulate the $^4D_{7/2}$ level and decrease the intensity of the M2 and MIT lines. Thus, the presence of a magnetically insensitive, strong E1 transition limits the sensitivity to the magnetic field of any ratio involving the 257.26 Å line.

The most direct way to utilize the 257.26 Å transition to measure the magnetic field is to calculate the intensity ratio of the entire (E1+M2+MIT) blend with another bright Fe X line as a function of the magnetic field after the plasma density has been measured, and compare it with observation. This is the method developed by Si et al. (2020a), who calculated the 174.53/257.26 intensity ratio and compared it with EIS observations.

There are two drawbacks with this method. The first one is given by the presence of the magnetically insensitive E1 transition, which accounts for a large fraction of the 257.26 Å intensity and thus severely limits its sensitivity to the magnetic field: for example, the 174.53/257.26 intensity ratio utilized by Si et al. (2020a) changes by ≈15% as the magnetic field ranges from 0 to 1000 G.

The second one lies in the use of the 174.53 Å and 175.26 Å lines to determine both the electron density and the magnetically sensitive ratio. In principle, the choice of this line pair has two big advantages: first, it is the most density-sensitive ratio in the EUV Fe X spectrum; second, these two lines are very bright. However, they are located in wavelength at the edge of the EIS passband, leading to their signal-to-noise ratio (S/N) being low in EIS observations. Therefore, they are seldom included in the line selection to be telemetered down from the Hinode satellite. This is especially true when images of the magnetic field in active regions are sought, for which rebinning can be limited, and thus, even if available, the 174.53 Å and 175.26 Å may have too-low S/N. Thus, while the approach in itself is powerful, it can only be applied to a limited number of EIS observations.

To improve on the sensitivity of the magnetic field diagnostic technique proposed by Si et al. (2020a) and to extend its applicability to a large fraction of observations carried out by EIS during its 14 yr long mission, we introduce here two different methods to utilize the magnetic properties of the MIT transition. Both methods rely on separating the MIT transitions from the contributions of the E1 and, when possible, also the M2 transition. Also, we use the Fe X 184.54 Å line in place of the 174.53 Å and 175.26 Å lines used by Si et al. (2020a): the former is one of the brightest lines in the Fe X spectrum, and most importantly one of the most commonly observed lines in the entire EIS data set.

For both techniques, it is important to realize what is the effect of the magnetic field on the population of the $^4D_{7/2}$ level. This level is metastable, so at electron densities lower than $\approx 10^9$ cm^{-3} it is only depopulated by M2 radiative transitions. As the electron density increases, collisional depopulation competes with radiative decay until, at $N_e \approx 10^{10}$, the former process dominates. Beyond this density, the $^4D_{7/2}$ level population and the intensity of the M2 transition rapidly decrease. The presence of the additional, magnetically induced radiative channel giving rise to the MIT transition increases the efficiency of radiative depopulation and pushes to higher values the density at which electron collisions begin to affect the level population and decrease the intensity emitted by the $^4D_{7/2}$ level.

On the other side, both the MIT and M2 transitions originate from the same level, so as the MIT A-value increases with the magnetic field, the relative intensity of the MIT transition increases at the expense of the M2 transition. These properties allow us to define two different techniques that apply to different magnetic field regimes.

2.4. Weak Magnetic Field Technique

When the magnetic field is weaker than ≈150–200 G, the A-value of the MIT transition is still smaller than the M2 one. In this case, the presence of the MIT transition is not able to significantly affect the level population of the $^4D_{7/2}$ level, so line intensity ratios involving the M2 transition are still independent of the magnetic field. This property allows us to calculate the cumulative (E1+M2) contribution to the 257.26 Å line using line intensity ratios with other Fe X lines calculated with the CHIANTI database (Dere et al. 1997, 2019), neglecting the magnetic field. The (E1+M2) contribution can be used to directly determine the intensity of the MIT transition from the observed 257.26 Å intensity:

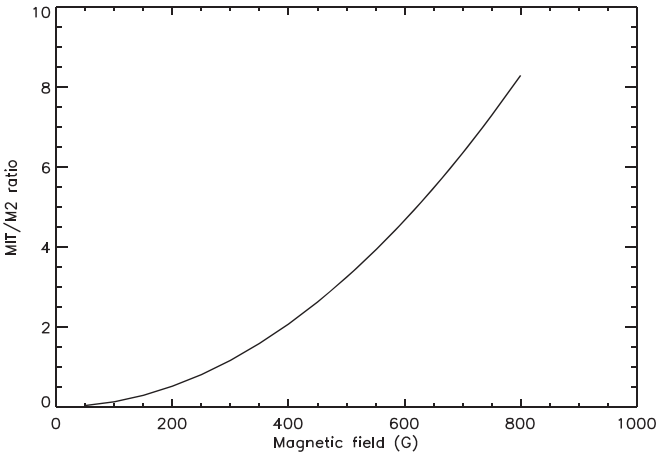

Figure 1. Intensity ratios as a function of magnetic field magnitude (in G). $I_{\rm MIT}/I_{M2}$ branching ratio, calculated in the low-density limit.

$$I_{\rm MIT} = I_{257} - I_{184} \times R[(E1 + M2)/184] \quad (1)$$

where I_{257} and I_{184} are the measured intensities for the 257.26 Å and 184.54 Å lines, respectively, and $R[(E1 + M2)/184]$ is the intensity ratio predicted by CHIANTI including both the E1 and M2 components, but not the MIT one. In other words, Equation (1) measures the excess emission in 257.26 Å that CHIANTI cannot account for with only the M2 and E1 transitions.

In a similar way, the intensity I_{M2} of the M2 transition can be directly determined as

$$I_{M2} = I_{184} \times R[M2/184] \quad (2)$$

where $R[M2/184]$ is the ratio between the M2 component and the 184.54 Å line, also predicted by CHIANTI. The ratio $I_{\rm MIT}/I_{M2}$ can then be directly compared with the branching ratio predicted by Li et al. (2015), as shown in Figure 1:

$$\frac{I_{\rm MIT}}{I_{M2}} = \frac{I_{257}}{I_{184}} R[184/M2] - R[(E1 + M2)/M2] \quad (3)$$

There are two main limits to this technique. First, the electron density tends to limit the sensitivity of this ratio. In fact, as the electron density increases, the intensity of the M2 transition decreases as collisional deexcitation increasingly competes with the M2 and MIT radiative decays to depopulate the $^4D_{7/2}$ level at densities larger than $N_e = 10^9$ cm^{-3}. For this reason, the signatures of the MIT transition in Equation (3) become very small, so the CHIANTI estimate of the MIT/M2 branching ratio loses sensitivity to the field strength. At densities typical of active regions ($\log N_e$ in the 9.0–9.5 range), this technique is sensitive to field strengths larger than ≈50 G. At densities typical of quiet Sun conditions ($\log N_e$ in the 8.0–8.5 range), the sensitivity threshold decreases to 10–20 G. As magnetic field strengths approach this limit, the branching ratio shown in Figure 1 leads to an overestimation of the magnetic field.

Second, when the magnetic field is larger than ≈150–200 G, the MIT transition rate grows large enough to affect the level population of the $^4D_{7/2}$ level and the M2 line intensity itself. In this case, the M2/184 ratio in Equation (2) also depends on B, so $I_{\rm MIT}/I_{M2}$ cannot be calculated neglecting the presence of B.

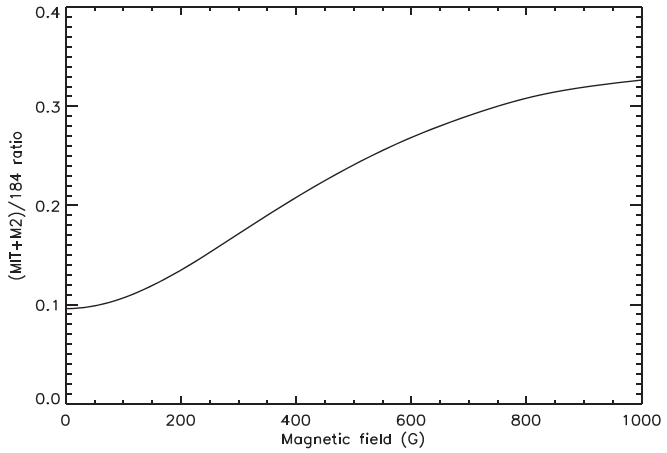

Figure 2. I_{M2+MIT}/I_{184} intensity ratio calculated as a function of magnetic field magnitude, in gauss.

Also in this case the weak-field technique leads to an overestimation of the magnetic field.

2.5. Strong Magnetic Field

When the magnetic field is stronger than 150–200 G, the M2 intensity also depends on the magnetic field, and the weak-field technique cannot be applied. However, the effect of the MIT transition on the overall Fe X level population is limited regardless of the magnetic field strength, so other intensity ratios involving Fe X lines still are independent of B. This allows us to determine the E1 transition intensity from the measured 184.54 Å line intensity:

$$I_{E1} = I_{184} \times R[E1/184] \tag{4}$$

where $R[E1/184]$, also calculated by CHIANTI, is the ratio between the E1 component and the 184.54 Å line. This ratio depends on the magnetic field by less than 25% at any value of the magnetic field. In this way, the intensity ratio

$$\frac{I_{M2+MIT}}{I_{184}} = \frac{I_{257} - I_{184} \times R[E1/184]}{I_{184}} = \frac{I_{257}}{I_{184}} - R[E1/184] \tag{5}$$

can be calculated with CHIANTI and compared with observations to measure B. One example is shown in Figure 2. It is important to note that while this ratio is less sensitive to the field strength than the $MIT/M2$ branching ratio is, it is still more sensitive to B than the ratio proposed by Si et al. (2020a) as the intensity of the magnetically insensitive E1 transition is removed from the measured one. However, the sensitivity of the ratio in Equation (5) decreases at lower densities, so below 10^9 cm^{-3} there is no advantage of this technique over the one proposed by Si et al. (2020a). Above this limit, the strong-field limit method is more sensitive and can be applied in active regions, where the magnetic field can easily be larger than 200 G and densities exceed 10^9 cm^{-3}.

2.6. Intensity Calibration

Both the weak-field and strong-field techniques rely on line intensity ratios. Thus, the absolute intensity calibration is not as important as the relative intensity calibration between the lines involved in the ratios. Since the only spectrometer currently able to measure the spectral lines needed to carry out the techniques outlined above is EIS, the relative calibration of this instrument is of critical importance.

A critical point to note is that the 257.26 Å line is the only strong Fe X line in the EIS long-wavelength (LW) detector, while all others are observed in the short-wavelength (SW) one. This makes the relative calibration of the two detectors a critical factor in the measurement of coronal magnetic fields. The EIS intensity calibration was measured before launch (Lang et al. 2006), but it has been subsequently revised to account for inaccuracies and a sensitivity decrease with time. Unfortunately, two competing calibrations have been produced (see Warren et al. 2014 and del Zanna 2013 for HPW and GDZ, respectively), which provide different relative SW/LW calibration factors, which in addition depend on time in a different way. This provides a critical uncertainty to the present measurements, which will also be discussed in Section 5.

2.7. Plasma Density

All of the intensity ratios involving one among the E1, M2, and MIT transitions and any other Fe X line are sensitive to the electron density N_e, the sensitivity being largest when $N_e > 10^9$ cm^{-3}, typical of active regions. Thus, an independent estimate of the electron density is necessary for both techniques. Si et al. (2020a) chose the best line ratio to carry out the estimate, namely the 174.53/175.26 ratio. This ratio should be used whenever possible. However, since Hinode/EIS observations have low S/N for the 174.53 Å and 175.26 Å lines and often do not include them, it is often necessary to use another ratio.

The other Fe X lines in the EIS range are weaker, and while a few individual observations can include them, they cannot be used for extensive application to magnetic field measurements, and thus it is necessary to resort to density-sensitive ratios from other ions. These ions need to be formed close in temperature to Fe X and need to provide line pairs with strong lines routinely observed and telemetered down by EIS. The best candidate is the Fe XI 182.17/(188.22+188.30) line ratio. These Fe XI lines are strong and extensively included in EIS observing sequences; the 188.2 doublet is only partially resolved by EIS, but its intensity can be easily measured either by a double Gaussian fit or simply by summing all of the counts under the profile and subtracting the background. This doublet is sufficiently strong and isolated to allow for both options. These lines are stronger than those available for density diagnostics in the EIS line list for Fe IX—the other closest Fe ion—or for ions of other elements.

In principle, the Fe VIII 185.21/186.60 intensity ratio can also be used as a density diagnostic to measure the magnetic field in cold, isolated loop structures when no other lines are present. Both of these lines are bright and isolated, are often telemetered to the ground, and provide a density-sensitive diagnostic line pair. However, care should be taken in checking that the spatial distribution of the intensity of Fe VIII and Fe X is the same, to minimize errors and to make sure that the emitting plasma is the same and the temperature difference between these two ions is not a problem. Similar caution needs to be taken when using the other line pairs commonly included in EIS observing sequences: Fe XII 186.8/195.1 and Fe XIII 203.8/202.0. Both of these ions are formed at a significantly higher temperature than Fe X is. We discuss the uncertainties that are due to electron density determination in Section 5.

Table 1
Hinode/EIS Observing Sequences Suitable for Coronal Magnetic Field Diagnostics

Acronym	FOV (arcsec^2)	Exp. Time (s)	Slit (arcsec)	Full Spectrum	Notes
AKATSUKI_01_SI	45 × 512	240	1	Y	
arm_loop_ne	82 × 400	25	2		
AR_velocity_map	330 × 304	40	1		
AR_velocity_map_v2	459 × 384	40	1		
AR_spectral_atlas_3	120 × 120	40	2	Y	
Atlas_060x512_45s	60 × 512	45	1	Y	
Atlas_060x512_60s	60 × 512	60	1	Y	
Atlas_30	120 × 160	30	2	Y	
Atlas_60	120 × 160	60	2	Y	
Atlas_120	120 × 160	120	2	Y	
cam_artb_cds_a_lite	200 × 400	10	2		
cam_artb_lite_v2	40 × 120	10	2		
cam_ar_limb_lite_v2	323 × 376	45	2		
cam_ar_temp_lite	359 × 400	30	2		
cam_qs_2as_velo	20 × 200	15	2		
cam_qs_2as_context	120 × 360	30	2		
cavity_dem_1	302 × 352	100	2		Fe VIII
CLASP-1_60x512_OBS_	60 × 512	60	2		
CLASP-1_60x512_CAL_	60 × 512	60	1		
CompS_NonMax_120	80 × 512	120	2		
CompS_NonMax_90	80 × 512	120	2		
CompS_NonMax_60	80 × 512	120	2		
CompS_NonMax_30	80 × 512	120	2		
COMSCI_QS5	10 × 512	5	1	Y	
Cool_loop_response	90 × 144	20	2		Fe VIII
Coronal_rain_1as2pos	40 × 256	10	1		Fe VIII
dhb_atlas_30x512	60 × 512	120	2	Y	
dhb_atlas_120m_30"	60 × 160	120	2	Y	
DIAG_40x180_s0_30s	40 × 176	30	2		
dob_bp_slit_raster	120 × 160	30	2		Fe XII
DRW001_HI_BRT_SCAN	5 × 240	60	1		
DRW001_HI_BRT_V2	5 × 240	30	1		
DRW001_HI_BRT_V3	10 × 240	30	1		
Eclipse_raster_v2	180 × 176	30	2		

Note. Sequences where density diagnostics from Fe XI are unavailable but are provided by Fe VIII or Fe XII ratios are indicated in the far-right column.

3. Observations

3.1. EIS Observing Sequences Suitable for Magnetic Field Diagnostics

In order to test the magnetic field diagnostic technique, we produced magnetic field maps on several active regions observed during the entire EIS mission. The results we report in this paper are just a drop in the ocean, as the EIS mission has developed plenty of observing sequences that include the necessary lines to carry out magnetic field measurements. In order to help users select suitable sequences to measure the coronal magnetic field, a list of these sequences is reported in Tables 1–3. The vast majority of them include either the entire Hinode/EIS spectrum or the four Fe X and Fe XI lines we used to carry out the present diagnostics. We also report a few more where Fe XI density diagnostics are not available, but either the Fe VIII 185.2/186.6 or Fe XII 186.8/195.1 ratio is available: these sequences may also be used for magnetic field diagnostics, although care must be taken in ensuring that the plasma structures observed by Fe VIII,X,XII are the same. We hope that this list will be useful to the reader to identify data sets suitable for measurements of the magnetic field in the solar corona.

3.2. Data Used in the Present Work

For the present work, we only selected a few observations, requiring that their fields of view include an active region and that they include all four Fe X and Fe XI lines to carry out the present diagnostics. We also selected a few more to check the effects of using Fe XI density and detector degradation effects later in the mission. These observations are listed in Table 4. These images were cleaned and calibrated using the standard EIS software. In addition, the detector slant was corrected so that the images obtained in the LW and SW were coaligned.

Very careful considerations were made in the choice of the intensity calibration. The GDZ calibration was determined by monitoring a large number of line intensity ratios from the beginning of the EIS mission, and the author made extensive comparisons with high-accuracy line intensity measurements available in the literature. The HPW calibration attempted to improve on the GDZ calibration by relying on extensive plasma diagnostic measurements in near-isothermal quiet regions rather than on individual line intensity ratios, by tying the EIS calibration to independent measurements from the EUV Variability Experiment (EVE; Woods et al. 2012) and the Atmospheric Imaging Assembly (AIA; Lemen et al. 2012) on board the Solar Dynamic Observatory (SDO; Pesnell et al. 2012), and by also trying to

Table 2
Hinode/EIS Observing Sequences Suitable for Coronal Magnetic Field Diagnostics

Acronym	FOV (arcsec^2)	Exp. Time (s)	Slit (arcsec)	Full Spectrum	Notes
EL_FULL_CCD_RASTER	14 × 512	300	2	Y	
EL_FULL_CCD_SINGLE	4 × 512	300	2	Y	
EL_abund_plume_SUMER	46 × 512	100	2		Fe VIII
EL_loop_plume_SUMER	61 × 512	100	2		
el_loop_diagn_sumer	61 × 280	50	1		
EL_WHI_CH_small	62 × 120	100	2		
EL_WHI_CH_LIMB	2 × 512		2	Y	
EL_SUMER_UVCS	2 × 400	150	2	Y	
EUNIS_EIS_CrossCal18	122 × 512	50	2		
FILL001	1 × 256	30	2	Y	
FELDMAN_QSCH_ATLASv1	60 × 304	120	2	Y	
FOCUS_STUDY	60 × 512	90	1		Fe XII
fullccd_sns30	2 × 160	30	2		
fullccd_scan_m30	120 × 160	30	2	Y	
GDZ_300x384_S2S3_40	300 × 384	40	2		
GDZ_DENS_20x240_ARL1	20 × 240	10	2		
GDZ_DENS_20x240_ARL2	20 × 280	15	2		
GDZ_360x288_AR_CONT2	360 × 288	6	2		Fe XII
GDZ_PLUME1_2_300_150	300 × 512	150	2		
GDZ_PLUME1_2_300_50s	300 × 512	50	2		
gdz_off_limb1_60	487 × 512	60	2		
GDZ_QS1_60x512_60s	60 × 512	60	2		Fe XII
HH_QS_RAS_N01	60 × 120	60	1	Y	
HH_QS_RAS_H01	41 × 120	60	1	Y	
HPW001_FULLCCD_RAST	128 × 128	90	1	Y	
HPW001_FULLCCD_V2	26 × 456	90	1	Y	
HPW008_FULLCCD_RAST	128 × 128	25	1	Y	
HPW008_FULLCCD_V2	128 × 256	25	1	Y	
HPW009_FULLCCD_SAS	1 × 128	25	1	Y	
HPW020_VEL_FULLs1	1 × 512	120	1	Y	
HPW023_FULLCCD_V2	1 × 512	300	1	Y	
HPW023_FULLCCD_V2s2	2 × 512	300	2	Y	
HPW023_FULLCCD_V3s2	2 × 512	100	2	Y	
HPW023_FULLCCD_300s	1 × 512	300	1	Y	

Note. Sequences where density diagnostics from Fe XI are unavailable but are provided by Fe VIII or Fe XII ratios are indicated in the far-right column.

calibrate the SW and LW detectors by making measurements of the Fe XXIV 192/255 line intensity ratio during flares agree with their predicted values.

No definitive conclusion can be reached regarding which of the two calibrations is most accurate. However, the GDZ calibration assumes that the LW channel did not decrease its sensitivity with time after 2012, while the HPW calibration assumes a continuous decrease. A monitoring of the Fe XIV 211.32/274.20 line intensity ratio from 2007 to 2020 indeed shows an initial decrease in relative sensitivity of the LW channel until 2012 and a subsequent flattening of the ratio (H.P. Warren, private communications), indicating that the GDZ calibration is more accurate after 2012. In this work, we preferred the GDZ calibration over the HPW one for three reasons: (1) no other systematic study has been published after 2014 that provides a definitive answer on the EIS calibration, (2) the GDZ calibration is likely more accurate after 2012, and (3) we preferred consistency. We will discuss the effects of the calibration choice in Section 5.

Line intensities were determined by summing the number of counts under the line profile and subtracting the background, determining the latter from regions of the spectrum very close to each line devoid of any other line. While such a method provides reasonably good estimates of line intensities for isolated lines (and for the 188 doublet), it needs to be tested for the 257.26 Å line. In fact, this line is surrounded by several other spectral lines that, though resolved, partially mask the wings of the Fe X transition. While the 257.26 Å line is stronger than all of them, extensive tests were run to ensure that the intensities measured in this way are within a few percent of the intensities calculated by fitting Gaussian profiles to both the Fe X and other nearby lines.

In measuring line intensities, no spatial averaging was performed, in order to preserve the original spatial resolution of the EIS observations. Even if averaging would have reduced the noise in the magnetic field determination, we preferred to maintain the original resolution to stress the ability of this method to provide high-resolution magnetic field maps.

4. Results

Since this technique simply consists of determining the excess emission in 257.26 Å, in principle it can be applied to all of the EIS observing sequences that include this line, a reference Fe X line, and a suitable density-diagnostic line pair to measure the electron density with. While not all EIS observing sequences have all these required lines, observations that include them span the entire EIS mission. As such,

Table 3
Hinode/EIS Observing Sequences Suitable for Coronal Magnetic Field Diagnostics

Acronym	FOV (arcsec^2)	Exp. Time (s)	Slit (arcsec)	Full Spectrum	Notes
iiap_ch_sns_v2	2 × 512	60	2		Fe VIII,XII
iiap_ch_ctxt_v2	120 × 512	60	2		
KM_FULLCCD_128x256_1slit_80sec	128 × 256	80	1	Y	
KM_FULLCCD_128x512_1slit_80sec	128 × 512	80	1	Y	
kpd_01_qs_60s	56 × 512	60	1		Fe VIII,XII
LANDI_SCAN_CH	60 × 512	240	2		
Large_CH_Map	180 × 512	60	2		Fe VIII,XII
madj_ech	120 × 512	60	2		Fe VIII,XII
madj_ech_small	24 × 512	60	2		Fe VIII,XII
prom_rast_v1	81 × 128	50	1		Fe VIII,XII
prom_rast_small_v2	4 × 128	25	1		Fe VIII,XII
PRY_CH_density	70 × 200	100	2		Fe VIII,XII
PRY_footpoints_v2	100 × 140	25	2		
PRY_footpoints_HI	180 × 512	25	2		
PRY_footpoints_HI2	180 × 512	25	2		
PRY_loop_footpoints	100 × 216	30	2		
QS_atlas_offlimb	220 × 512	60	1		
RED_SUM_EIS_RAST	70 × 200	90	1		
RED_SUM_EIS_SNS_OL	70 × 200	90	1		
SI001FullRast	256 × 256	50	1	Y	
SI002_HiCadence_AR	280 × 512	50	1	Y	
SI_Mercury_slit	2 × 256	60	2	Y	
SI_Mercury_slit_v2	2 × 256	20	2	Y	
SI_Venus_slit	2 × 256	300	2	Y	
SI_Venus_slit_v2	2 × 256	100	2	Y	
SYNOP001	1 × 256	30	1	Y	
SYNOP002	128 × 184	90	1	Y	
SYNOP003	300 × 96	45	2	Y	
SYNOP004_400x400_30	400 × 400	30	2		
Utz_quiet	22 × 160	60	1		Fe XII

Note. Sequences where density diagnostics from Fe XI are unavailable but are provided by Fe VIII or Fe XII ratios are indicated in the far-right column.

applying this technique to this wealth of data is beyond the scope of this work; here we focus on presenting a few examples of this application and discuss their uncertainties.

4.1. Magnetic Field Evolution

Magnetic field strength maps allow us to monitor the short-term evolution of individual structures in an active region. An example of this is reported in Figure 3, where a weak active region with no number, which was trailing AR10980 at the solar equator, was repeatedly observed in 2008 January 10 to 15. During this time, the active region was observed for a total of 25 times and showed a marked evolution that led to no flares. The weakness of this active region allows for the use of the weak-field technique.

The high resolution of the EIS spectrometer allows us to identify individual plasma structures and monitor their evolution with time: we have identified the footpoint of a system of active-region fanning loops, which is highlighted in Figure 3 (top) by the black rectangle, and we measured the magnetic field of the selected box as a function of time. The magnetic field of this region looked very weak, as a pixel-by-pixel map of the coronal magnetic field of this region indicated the presence of a measurable field with a very poor S/N. In order to increase the S/N and attempt to measure the magnetic field strength in such a weak region, we have summed all of the counts for each spectral line within the box and applied the magnetic field diagnostic technique to the total line intensities.

The results are shown in Figure 3 (bottom). The uncertainties of each measurement are estimated to be ≈70% (see Section 5). The magnetic field is very weak, on the order of 30–150 G (thus confirming the use of the weak-field technique), and shows a vague tendency to decrease with time. The results tend to show some variability within the same cluster of observations (a couple of observations gave zero magnetic field strength), indicating that we are sampling the sensitivity limits of the present magnetic field diagnostic technique. This means that it will be very difficult to measure magnetic fields in the quiet Sun and even more so in coronal holes, where magnetic field strengths are smaller; the only places where such a measurement may be attempted with some hope of success are low-latitude locations at the solar limb, where the very long line of sight intercepts more plasma, increasing the S/N.

Another difficulty in carrying out such measurements is the evolution of the plasma structures themselves and the different viewing angles as they rotate on the solar disk. Both properties make the identification of an individual structure and its monitoring over long periods of time difficult and add to the uncertainty of the measurement.

4.2. Magnetic Field Morphology

An example of the application of the Fe X magnetic field diagnostic technique is shown in Figures 4–6. This set of observations, carried out between 2007 December 10 and 18, follows AR10978 as it rotated across the solar disk until

Table 4
Hinode/EIS Observations Used in the Present Work

Date	Time	FOV (arcsec^2)	Exp. Time (s)	Slit (arcsec)	Sequence	Full Spectrum
			Density Comparison			
2007 Jun 02	19:56:12	128 × 128	25	1″	HPW008_FULLCCD_RAST	Y
2010 Jun 21	14:24:01	120 × 160	60	2″	ATLAS_60	Y
			Magnetic Field Imaging			
2007 Dec 10	00:19:27	459 × 384	40	1″	AR_velocity_map_v2	N
2007 Dec 11	10:25:42	459 × 384	40	1″	AR_velocity_map_v2	N
2007 Dec 12	03:26:43	459 × 384	40	1″	AR_velocity_map_v2	N
2007 Dec 12	11:43:36	459 × 384	40	1″	AR_velocity_map_v2	N
2007 Dec 13	12:18:42	459 × 384	40	1″	AR_velocity_map_v2	N
2007 Dec 15	00:13:49	459 × 384	40	1″	AR_velocity_map_v2	N
2007 Dec 15	18:15:49	459 × 384	40	1″	AR_velocity_map_v2	N
2007 Dec 18	00:10:49	459 × 384	40	1″	AR_velocity_map_v2	N
2007 Dec 18	18:13:41	459 × 384	40	1″	AR_velocity_map_v2	N
			Time Variation Magnetic Field			
2008 Jan 10	18:07:32	180 × 512	25	2″	PRY_footpoints_HI	N
2008 Jan 10	22:51:03	180 × 512	25	2″	PRY_footpoints_HI	N
2008 Jan 11	00:16:33	180 × 512	25	2″	PRY_footpoints_HI	N
2008 Jan 11	00:57:03	180 × 512	25	2″	PRY_footpoints_HI	N
2008 Jan 11	01:37:32	180 × 512	25	2″	PRY_footpoints_HI	N
2008 Jan 11	02:18:02	180 × 512	25	2″	PRY_footpoints_HI	N
2008 Jan 11	03:39:02	180 × 512	25	2″	PRY_footpoints_HI	N
2008 Jan 11	04:31:24	180 × 512	25	2″	PRY_footpoints_HI	N
2008 Jan 11	05:30:47	180 × 512	25	2″	PRY_footpoints_HI	N
2008 Jan 11	06:11:17	180 × 512	25	2″	PRY_footpoints_HI	N
2008 Jan 11	07:11:06	180 × 512	25	2″	PRY_footpoints_HI	N
2008 Jan 12	13:20:33	180 × 512	25	2″	PRY_footpoints_HI	N
2008 Jan 12	14:01:04	180 × 512	25	2″	PRY_footpoints_HI	N
2008 Jan 12	14:41:34	180 × 512	25	2″	PRY_footpoints_HI	N
2008 Jan 12	15:22:04	180 × 512	25	2″	PRY_footpoints_HI	N
2008 Jan 14	12:00:33	180 × 512	25	2″	PRY_footpoints_HI	N
2008 Jan 14	13:21:30	180 × 512	25	2″	PRY_footpoints_HI	N
2008 Jan 14	14:02:00	180 × 512	25	2″	PRY_footpoints_HI	N
2008 Jan 14	14:42:30	180 × 512	25	2″	PRY_footpoints_HI	N
2008 Jan 14	21:30:02	180 × 512	25	2″	PRY_footpoints_HI	N
2008 Jan 14	22:10:31	180 × 512	25	2″	PRY_footpoints_HI	N
2008 Jan 15	00:18:32	180 × 512	25	2″	PRY_footpoints_HI	N
2008 Jan 15	11:24:25	180 × 512	25	2″	PRY_footpoints_HI	N
2008 Jan 15	12:04:54	180 × 512	25	2″	PRY_footpoints_HI	N
2008 Jan 15	12:45:24	180 × 512	25	2″	PRY_footpoints_HI	N
			LW Detector Degradation Effects			
2014 Mar 16	12:15:26	120 × 160	60	2″	ATLAS_60	Y
2016 Oct 25	11:33:15	120 × 160	30	2″	ATLAS_30	Y
2018 Dec 28	19:10:40	120 × 160	60	2″	ATLAS_60	Y

reaching the west limb. Despite the size and complexity, this active region was relatively quiet and hosted only a few C-class flares, although none of them took place while the observations were taken. Figures 4–6 show a snapshot of the Fe X 184.54 Å intensity map in the left column and the magnetic field map obtained with the present MIT diagnostic technique in the right column for each of the nine observation times. There are a few things to notice.

It is important to note that the magnetic field strengths in this region exceeded 200 G in most of its lowest-altitude and brightest structures, so the strong-field technique needed to be applied. However, the 50% uncertainty of the intensity calibration led this technique to provide uncertainties that were comparable to or even exceeded the range of sensitivity of the ratio shown in Figure 2, providing only a lower limit to the field strength. Thus, a precise determination of the field strength was not possible for the strongest magnetic fields, while for the weaker ones, especially at large heights, the weak-field technique could still be applied. In order to show the potential of this technique, we applied the weak-field technique everywhere even if the strongest magnetic field strengths are overestimated. Thus, even if the absolute values of the strongest magnetic field displayed in Figures 4 to 6 are inaccurate, these figures allow us to show the type of information that the presence of an MIT transition allows us to obtain from EIS observations.

First, the magnetic field structures shown in the figures closely follow the intensity maps of the Fe X line, as expected both on the grounds of a better S/N and that the magnetic field confines the active-region plasma, maintaining it at a higher density and temperature than the surrounding ambient plasma. Observations closer to the disk center allow reconstruction of several different loop structures connecting magnetic fields of opposite polarities, although the tallest loops become too faint as they rise to high altitude, such as those in the SW portion of

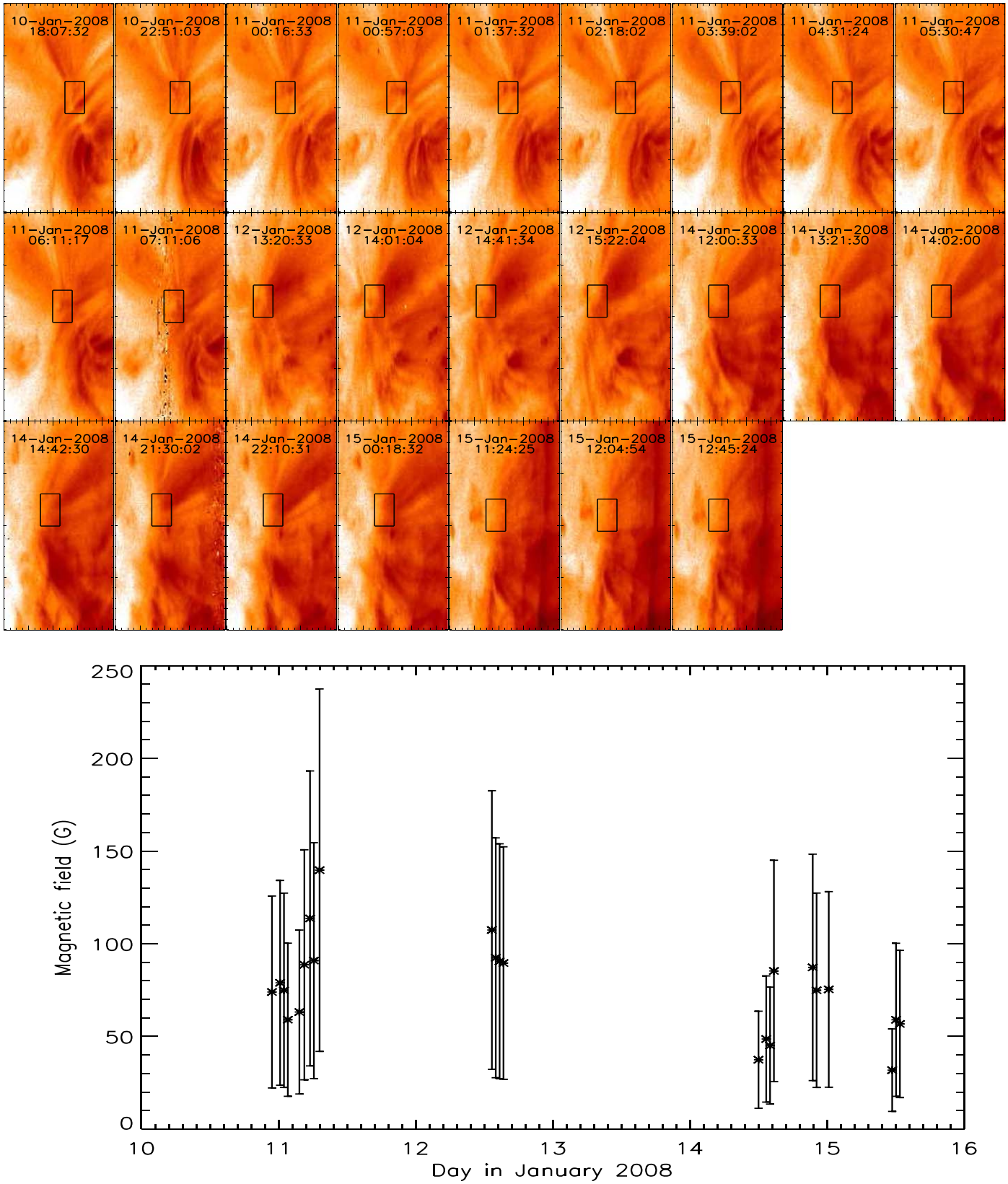

Figure 3. Magnetic field measurement for a weak active region observed in 2008 January 10 to 15. Intensities have been averaged over the reported boxes for each of the observations, and the magnetic field measurement has been carried out on the averaged intensities. Top panel: Fe X 184.54 Å intensity maps of a portion of the active region including the footpoints of fanning loops. Bottom panel: magnetic field strength measurements as a function of time.

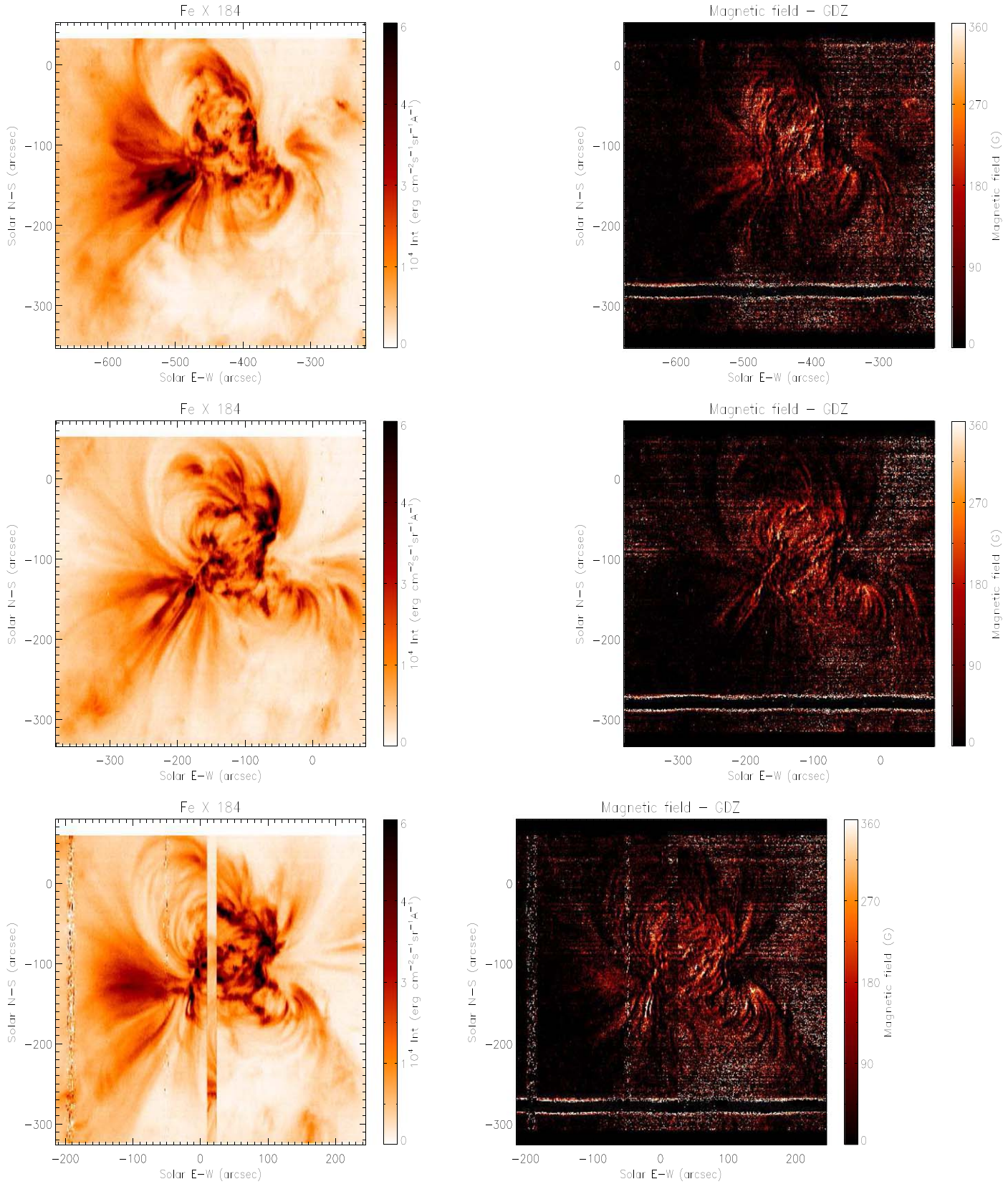

Figure 4. AR10978 maps on 2007 December: Fe X 184.54 Å intensity (left) and magnetic field strength (right). Observation days are December 10 (00:19:27 UT, top), December 11 (10:25:42 UT, middle), and December 12 (03:26:43 UT, bottom).

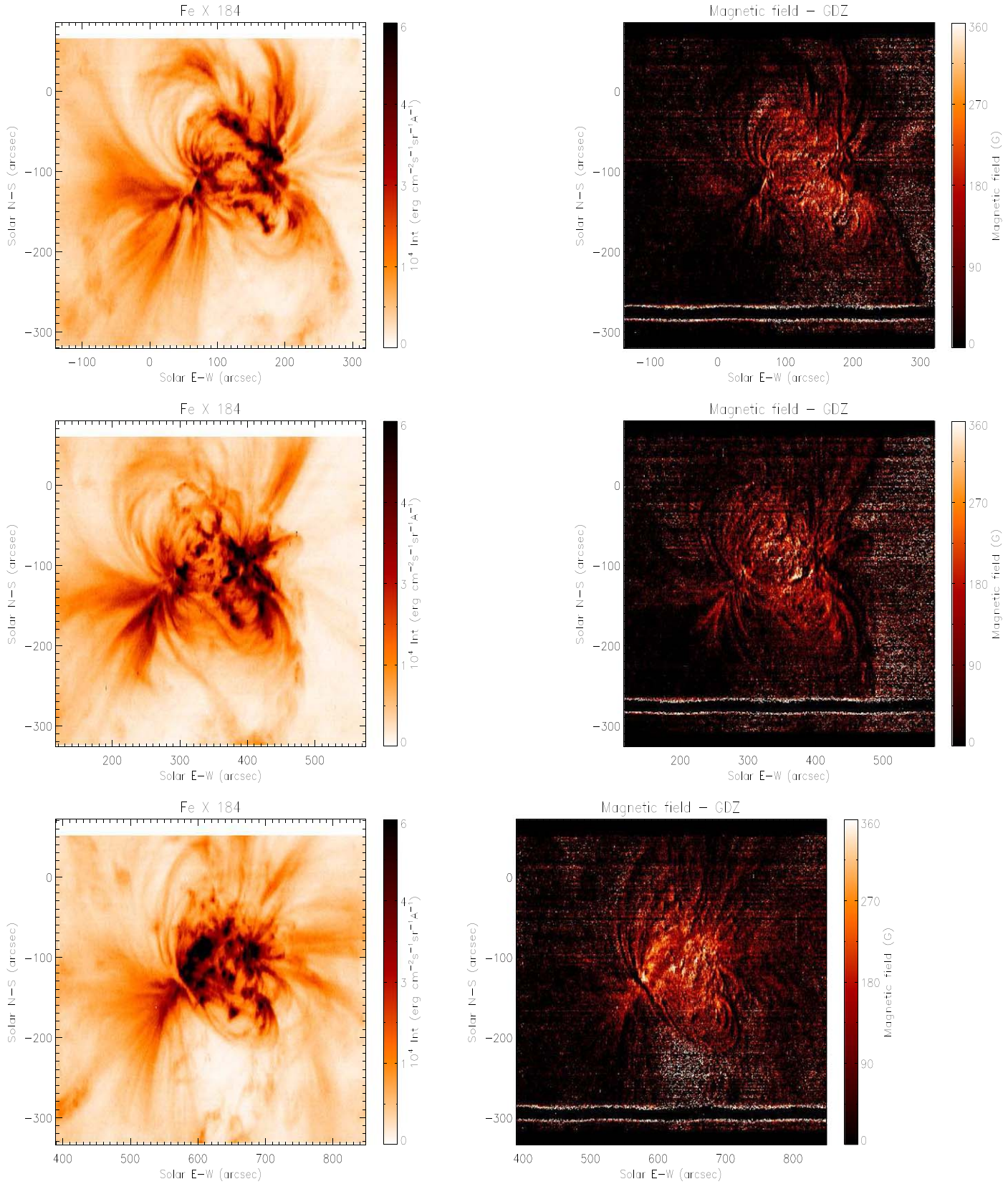

Figure 5. AR10978 maps on 2007 December: Fe X 184.54 Å intensity (left) and magnetic field strength (right). Observation days are December 12 (11:43:36 UT, top), December 13 (12:18:42 UT, middle), and December 15 (00:13:49 UT, bottom).

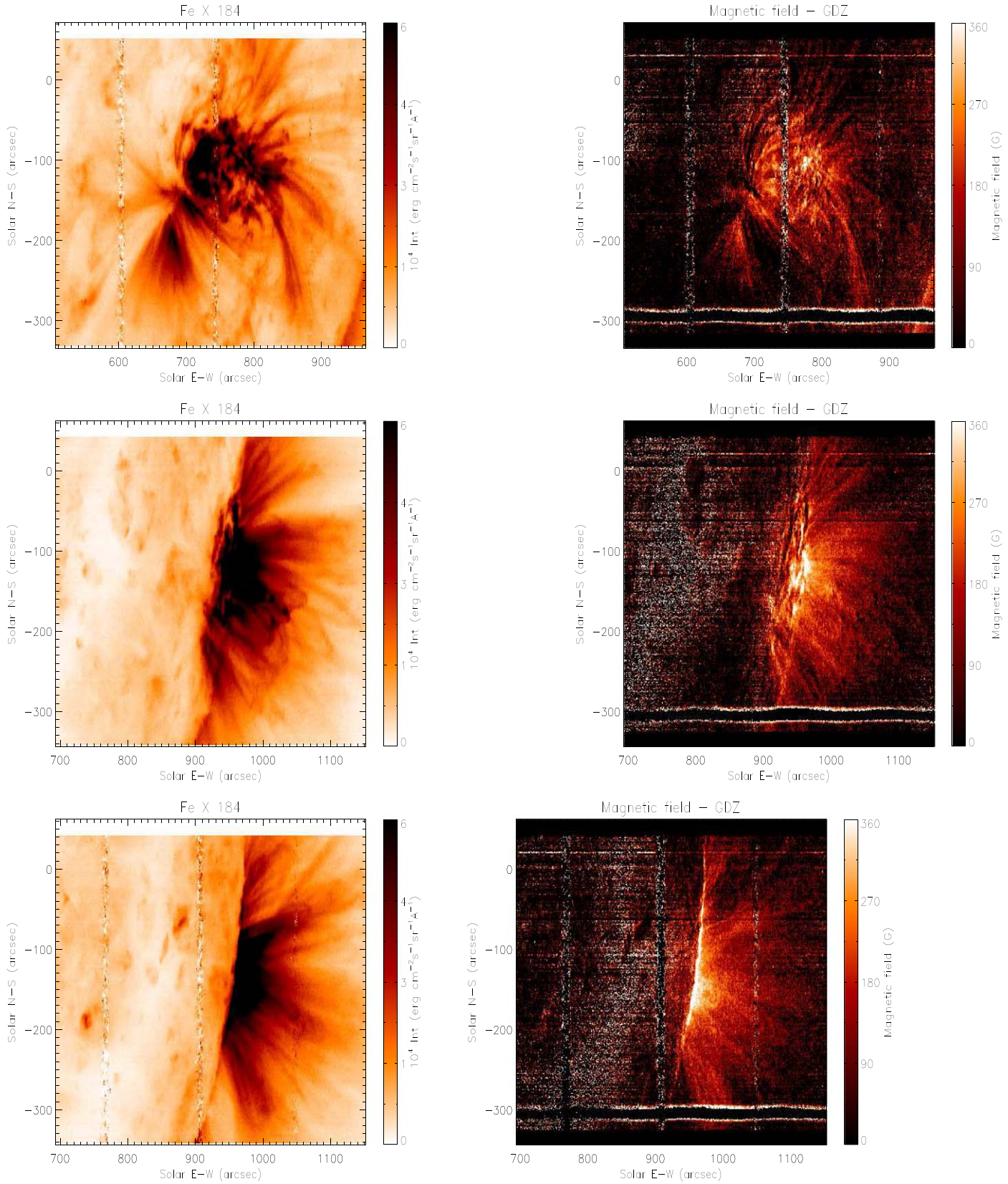

Figure 6. AR10978 maps on 2007 December: Fe X 184.54 Å intensity (left) and magnetic field strength (right). Observation days are December 15 (18:15:49 UT, top) and December 18 (00:10:49 UT, middle and 18:13:41 UT, bottom).

AR10978 in Figure 4, so they cannot be observed for the entirety of their length.

Second, even if the observations were taken only a few hours apart from each other, the magnetic field shows significant evolution, both in morphology and in strength, with magnetic loops changing position, appearing or disappearing from one observation to the next. This is consistent with the variability of line intensities and directly links the evolution of the field strengths with the plasma properties inside magnetic structures.

Third, the strength of the magnetic field is larger in low-lying loops than in larger loops. However, it is unclear whether the lower strength in large loops (leading to disappearance of the loops themselves at large heights) is due to a real weakening of the field with height or to a lower S/N. During the transit of AR10978 from disk center to the limb, the magnetic field strength steadily increases, consistent with the active region beginning to be more active and starting to host small C-class flares from December 13 (three C-class flares, the strongest of which is a C4.5 flare) until it turned behind the limb on December 19.

The variability of the magnetic field strength with height can be best monitored in Figure 6, where AR10978 is observed to be close to or at the limb. In these images, the strongest magnetic field is concentrated in the lowest-lying structures, closest to the surface, while taller loops have weaker fields. The tallest loops visible in the Fe X 184.54 Å image are barely visible in the magnetic field strength image, indicating either that their magnetic field is too weak to be detected or that the S/N is too low to allow this diagnostic technique to be effective. However, the very few closed-loop structures whose magnetic field strength is measurable at the limb for seemingly the whole loop length show a slowly varying magnetic field, which becomes weaker with height.

5. Uncertainties

5.1. Energy Level Separation

Despite the great potential for magnetic field diagnostics, the present technique has several uncertanties of a different nature. The first and most important is the intrinsic uncertainty in the calculation of the Einstein coefficient $A_{\rm MIT}$ for the magnetically induced transition. As discussed by Si et al. (2020b), to first order we can assume

$$A_{\rm MIT} \propto \frac{B^2}{(\Delta E)^2} \tag{6}$$

where ΔE is the energy separation between the two $^4D_{5/2,7/2}$ levels generating the 257.26 Å doublet. Measuring this energy separation is difficult because it is very small, and there are only a few spectral lines available that can be utilized, all very close in wavelength. Separating the two lines at 257.26 Å is essentially impossible as their separation is just a few milliangstroms, way below the resolution of the EIS instrument; also, the line width in the corona is way larger than this separation.

Note that ΔE can be measured using transitions where the $^4D_{5/2,7/2}$ levels are the lower levels of transitions coming from the same upper level, forming a doublet, as used by Judge et al. (2016). A few lines are available for this purpose. No laboratory or solar observations are available for a doublet at around 3500 Å, which would provide a separation of 0.65 Å, the 2935 Å doublet, and another doublet at 1611 Å. Only a few observations in the UV are available for the three other transitions remaining, at around 1918 Å, 1603 Å, and 1028 Å, the separation of the two lines being larger at longer wavelengths. Judge et al. (2016) utilized S082 spectra taken at the solar limb to measure the 1603 Å doublet separation through double Gaussian fitting, finding $\Delta E = 3.7 \pm 2.9\,{\rm cm}^{-1}$, so the uncertainty is around 80%. This uncertainty makes the technique capable of giving only the order of magnitude of the magnetic field strength.

More recently, Landi et al. (2020) have utilized the deep exposure of the quiet solar limb made with the high-resolution SoHO/SUMER spectrometer (Wilhelm et al. 1995) that provided the SUMER off-disk spectral atlas (Curdt et al. 2004); in this observation, Fe X 1463.49 Å was used to constrain the line width for all Fe X lines, helping reduce the ΔE uncertainty. Landi et al. (2020) determined a value of $2.29 \pm 0.50\,{\rm cm}^{-1}$. This uncertainty, at 20% level, greatly reduces the intrinsic uncertainty of any measurement of the magnetic field (see Equation (6)).

5.2. Electron Density

In order to apply the present magnetic field diagnostic technique, it is necessary to determine the plasma electron density independently. This can in principle be done using Fe X transitions, whose emission is generated by the same plasma emitting the 257.26 Å line. Si et al. (2020a) suggest the use of the two strong Fe X transitions at 175.26 Å and 174.53 Å: this choice is the most sensible, but these two lines are observed at the edge of the EIS SW detector, where the sensitivity is very low, and their intensities are highly uncertain. No other Fe X line ratios involving bright lines with high S/N are available in the EIS wavelength range. The next best solution is to utilize lines from ions formed at similar temperatures, and the best choice is Fe XI, as both Fe X,XI are ions formed in the corona only, while Fe IX receives strong contributions from colder, upper-transition-region plasmas likely not contributing to Fe X. Besides, Fe IX density-sensitive lines in the EIS spectrum are weaker and more difficult to observe and disentangle from nearby transitions. On the contrary, Fe XI provides strong, isolated lines that are routinely observed by the EIS spectrometer: 182.17 Å and the 188.22 + 188.30 Å doublet. The latter is actually a partially resolved doublet, but it is very strong and sufficiently isolated to make it very easy to measure.

However, using density measurements from another ion raises additional uncertainties: the emitting plasmas might not be the same, and thus the density measured by the two ions can be different. Figures 7 and 8 show intensity maps of two active regions in the Fe X 184.54 Å line and Fe XI 188.2 Å doublet, showing that indeed the two ions sample the same plasmas. These observations were taken as examples because they also included the 174.54 Å and 175.26 Å lines, so differences in both the density values and their spatial distribution could be checked. Both active regions clearly show the difficulty in observing the two Fe X 174.54 Å and 175.26 Å lines, due to the poor S/N, which is amplified in their ratio; still, the spatial distribution of the densest areas is the same as with the Fe XI density ratio. A detailed comparison of density measurements over restricted areas shows that these two ratios are within $\Delta \log N_e \approx 0.1$ in the brightest areas, where the magnetic field measurements will be most accurate.

Density values in Figures 7 and 8 are in the $\log N_e = 9.0$–9.5 range, typical of active regions, where the emissivity ratios involved in Equations (1) and (2) are also density sensitive. Electron density thus contributes to the overall uncertainty in

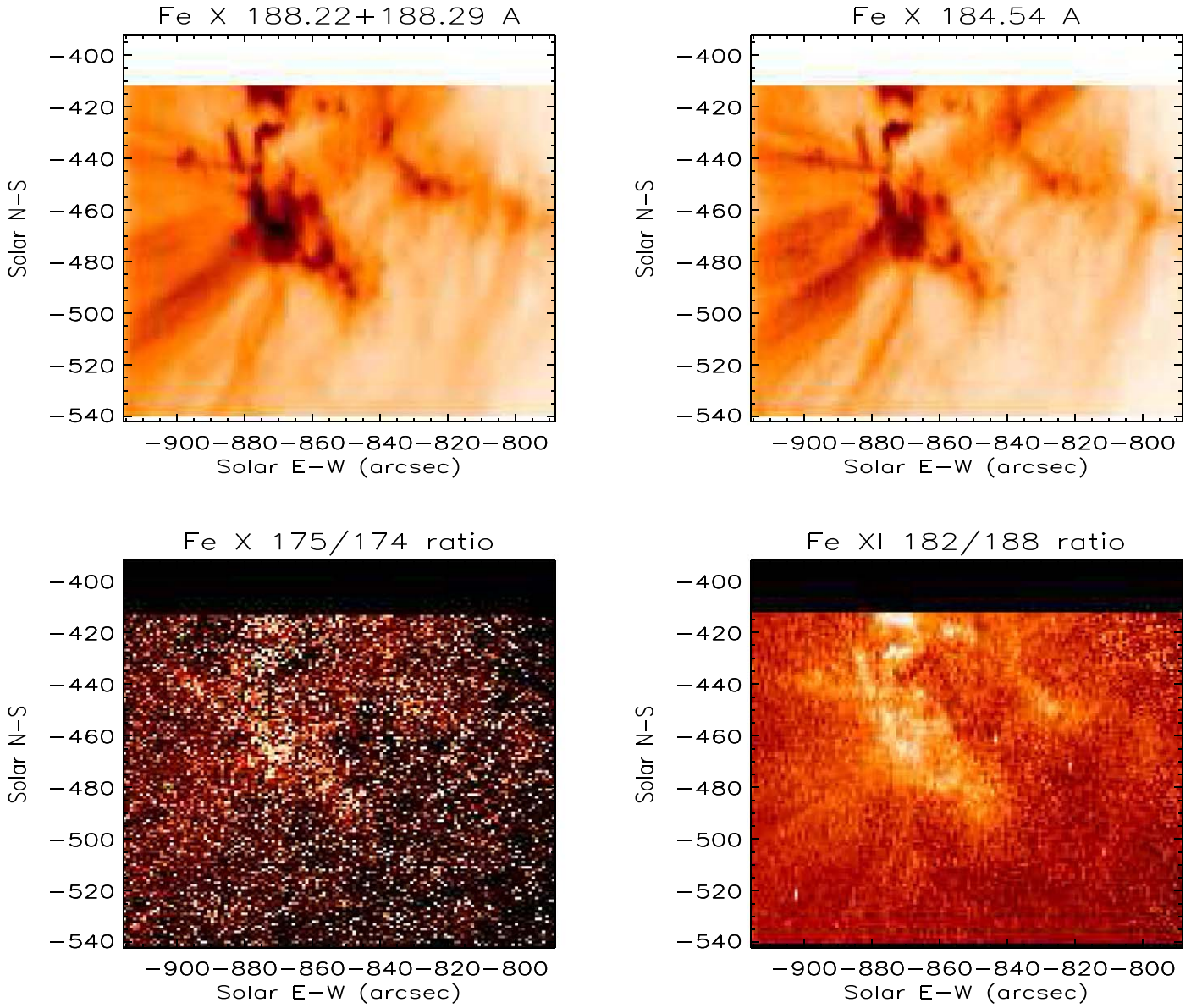

Figure 7. EIS observations of AR10960 observed on 2007 June 2. Top: intensity maps obtained with the Fe XI 188.2 Å doublet and the Fe X 184.54 Å line. Bottom left: density map obtained with the Fe X 175.26/174.54 intensity ratio; bottom right: density map obtained with the Fe XI 182/188 intensity ratio.

the measurement of the magnetic field strength. The line intensity ratios we propose to use in this technique can provide measurements of the electron density down to 0.1 dex uncertainty, corresponding to roughly 25% of the measured density: this uncertainty propagates into the emissivity ratios, providing an uncertainty of ≈15% that needs to be considered in the final uncertainty of the measured magnetic field. An additional uncertainty of up to 20% may be introduced by a slight temperature sensitivity of Fe X emissivity ratios, due to the temperature sensitivity of the collisional excitation rates. However, the temperature-related uncertainty can be eliminated by minimizing the thermal structure of the emitting plasma using standard plasma diagnostic techniques (see the review by Phillips et al. 2008).

5.3. Intensity Calibration

Calibration is another source of uncertainty of critical importance. The reason is that all of the strongest Fe X lines are located in the SW channel, while the magnetically sensitive 257.26 Å is located in the LW channel, so the relative calibration of the two is extremely important. Uncertainty in this parameter will directly propagate into the determination of both the weak-field and strong-field diagnostic ratios. Note that both these ratios depend on the I_{257}/I_{184} intensity ratio, rather than on absolute intensities, so the EIS absolute calibration is less important.

Two independent studies (HPW and GDZ) have been carried out to determine the in-flight EIS intensity calibration and compare it with the prelaunch one, from Lang et al. (2006).

The results showed that the preflight sensitivity of the LW channel was overestimated, but GDZ and HPW disagreed on the amount. Even more importantly, the LW channel showed a degradation with time relative to the SW channel, which directly impacts the present diagnostic technique. The wavelength dependence of the effective areas within each channel was largely the same as the preflight calibration, with the exception of the shortest wavelength of the SW channel (GDZ) or both ends of the SW channel (HPW): in both cases, the use

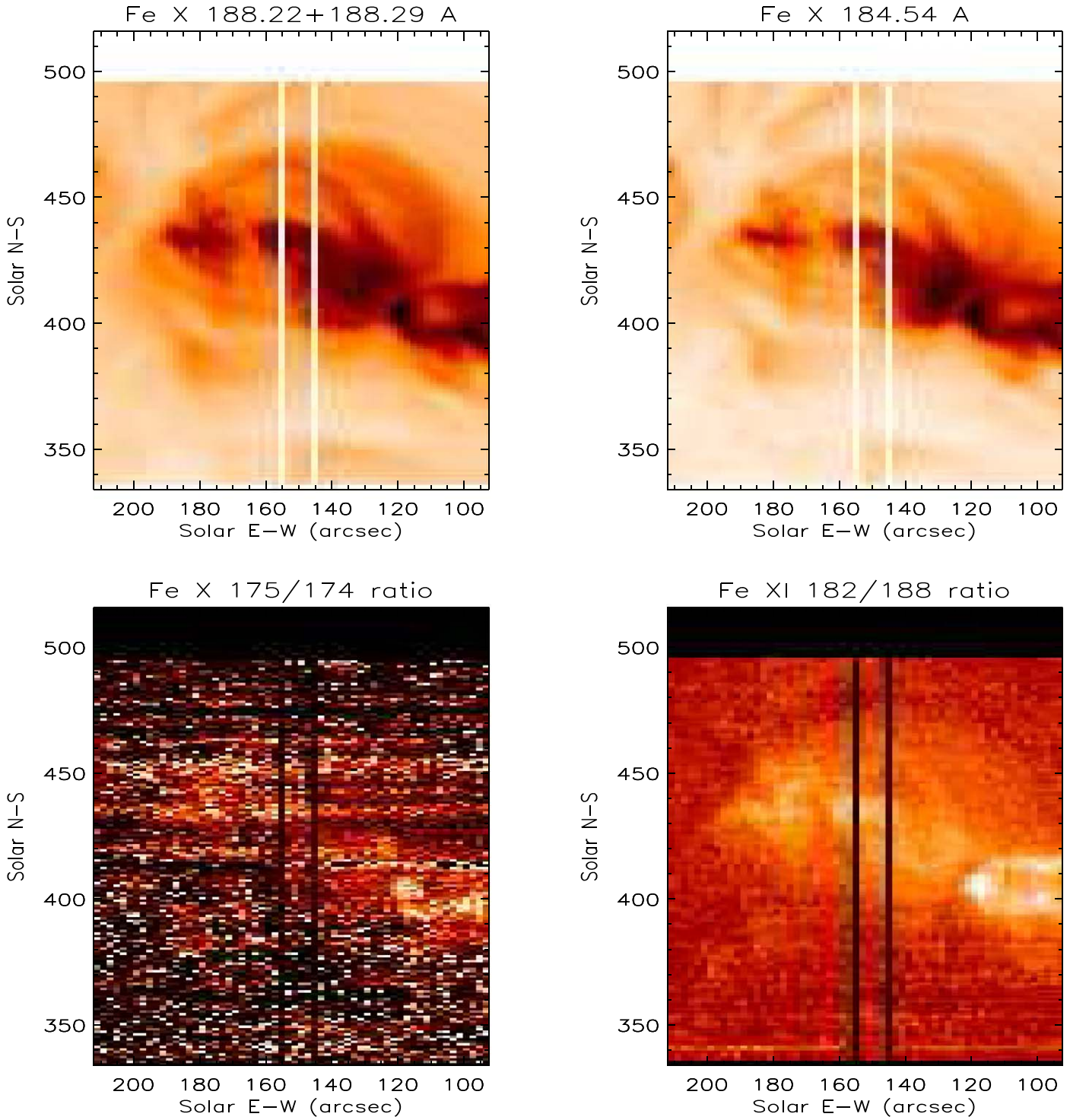

Figure 8. EIS observations of AR11082 on 2007 June 2. Top: intensity maps obtained with the Fe XI 188.2 Å doublet and the Fe X 184.54 Å line. Bottom left: density map obtained with the Fe X 175.26/174.54 intensity ratio; bottom right: density map obtained with the Fe XI 182/188 intensity ratio.

of the 174.53 Å line for the measurement of the magnetic field proposed by Si et al. (2020a) is significantly affected. Also, contradictory results were obtained when comparing the EIS absolute calibration with both the EVE instrument on board SDO and the EUNIS rocket flight (Wang et al. 2011).

There are multiple possible reasons for this discrepancy, because different methods, with their own strengths and weaknesses, are applied to different types of data and instruments. This is a general problem for in-flight calibration of high-resolution spectrometers (e.g., Landi et al. 1997, 1999; Young et al. 1998; del Zanna et al. 2001, 2010a). A noncomprehensive list of possible problems includes the following: (1) line intensity ratios are critically dependent on the quality of the atomic data and transition rates they depend upon, which changes from ion to ion; (2) analyses based on assumptions on the thermal structure depend on how much the plasma departs from these assumptions. Also, errors can be introduced by inaccurate effective areas when comparing narrowband imagers such as SDO/AIA 193, with spectrally

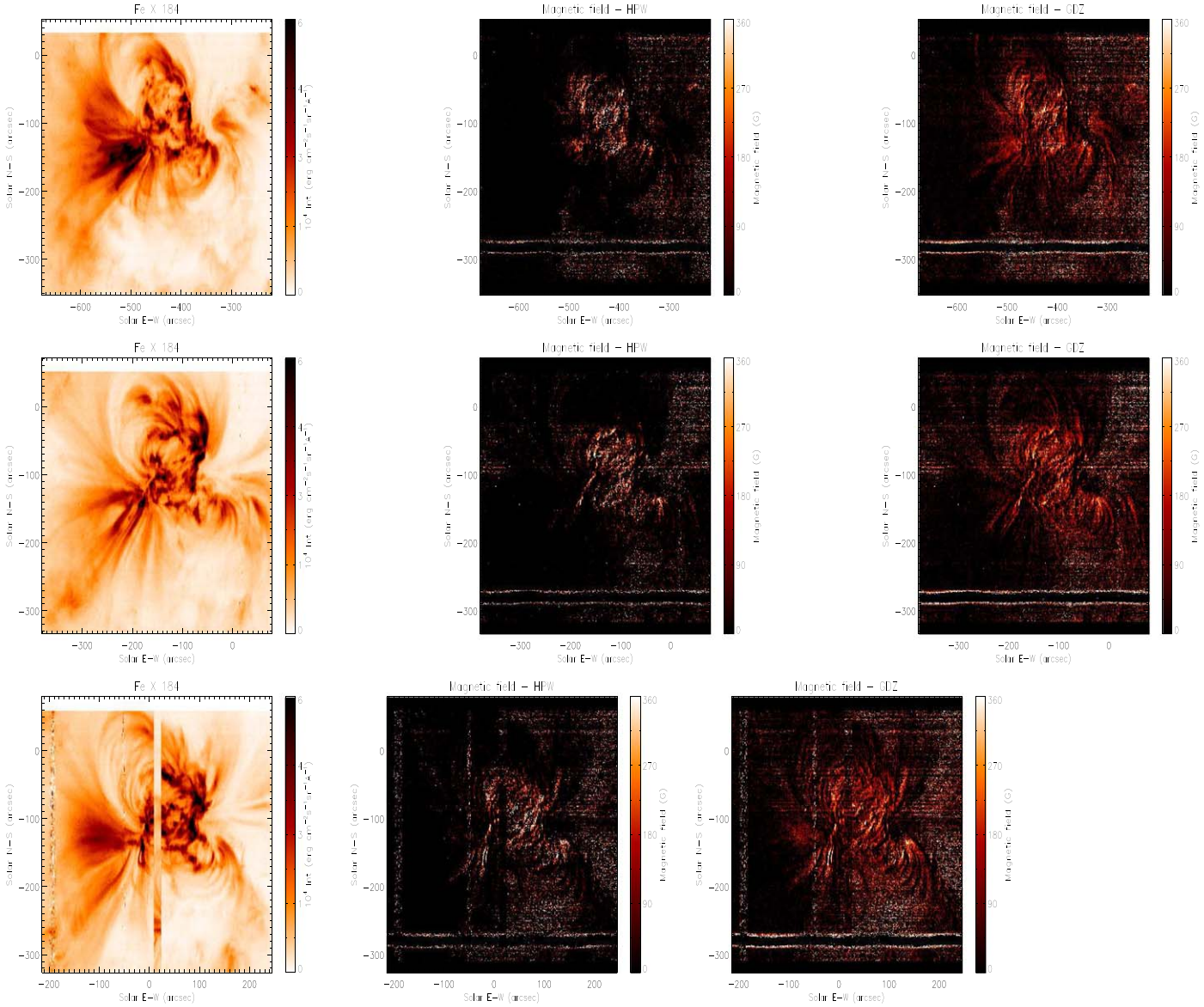

Figure 9. Comparison of magnetic field diagnostic results obtained with the HPW calibration (middle panels) and the GDZ calibration (right panels) from observations of AR10978.

resolved EIS spectra, or by intrinsic solar variability when monitoring the long-term changes in the intensities of cool, quiet Sun lines.

These uncertainties and discrepancies directly affect the present diagnostic technique. As discussed in Section 4.2, they caused the strong-field technique to provide only lower limits to the strongest fields, so we had to resort to the weak-field technique, even if the latter provided an overestimation of the field strength. Furthermore, even when using the weak-field technique, the effects of calibration uncertainties are still very large. An example of calibration-related uncertainties is shown in Figures 9 and 10, which display some of the data shown in Figures 4 to 6. The left panels show Fe X 184.54 Å intensity maps, and the middle and right panels show magnetic field strength measurements obtained with HPW calibration (middle panels) and GDZ calibration (right panels). As the scale of the magnetic field in both panels is the same, differences are apparent, with the HPW calibration leading to higher values for the stronger magnetic field and giving zero magnetic field strength for regions where the GDZ calibration provides small but measurable values of the magnetic field.

The present diagnostic technique essentially relies on the measurement of the 184.54/257.26 line intensity ratio. We estimate, based on the available EIS software, that the uncertainty in this ratio due to the intensity calibration is around 50% or less. This estimate takes into account also the variation of the intensity ratio due to detector degradation (see next section), which the EIS software takes into account.

5.4. EIS Detector Sensitivity Degradation

Figure 11 shows the results of applying the magnetic field diagnostic technique to data sets taken in later stages of the EIS mission, where the instrument sensitivity has already significantly decreased, especially for the LW channel, where the magnetically sensitive 257.26 Å line resides. Those results were obtained on full EIS spectra obtained with 60 s exposure time and the 2″ slit, a combination that at the beginning of the EIS mission ensured a very high S/N ratio. While the intensity

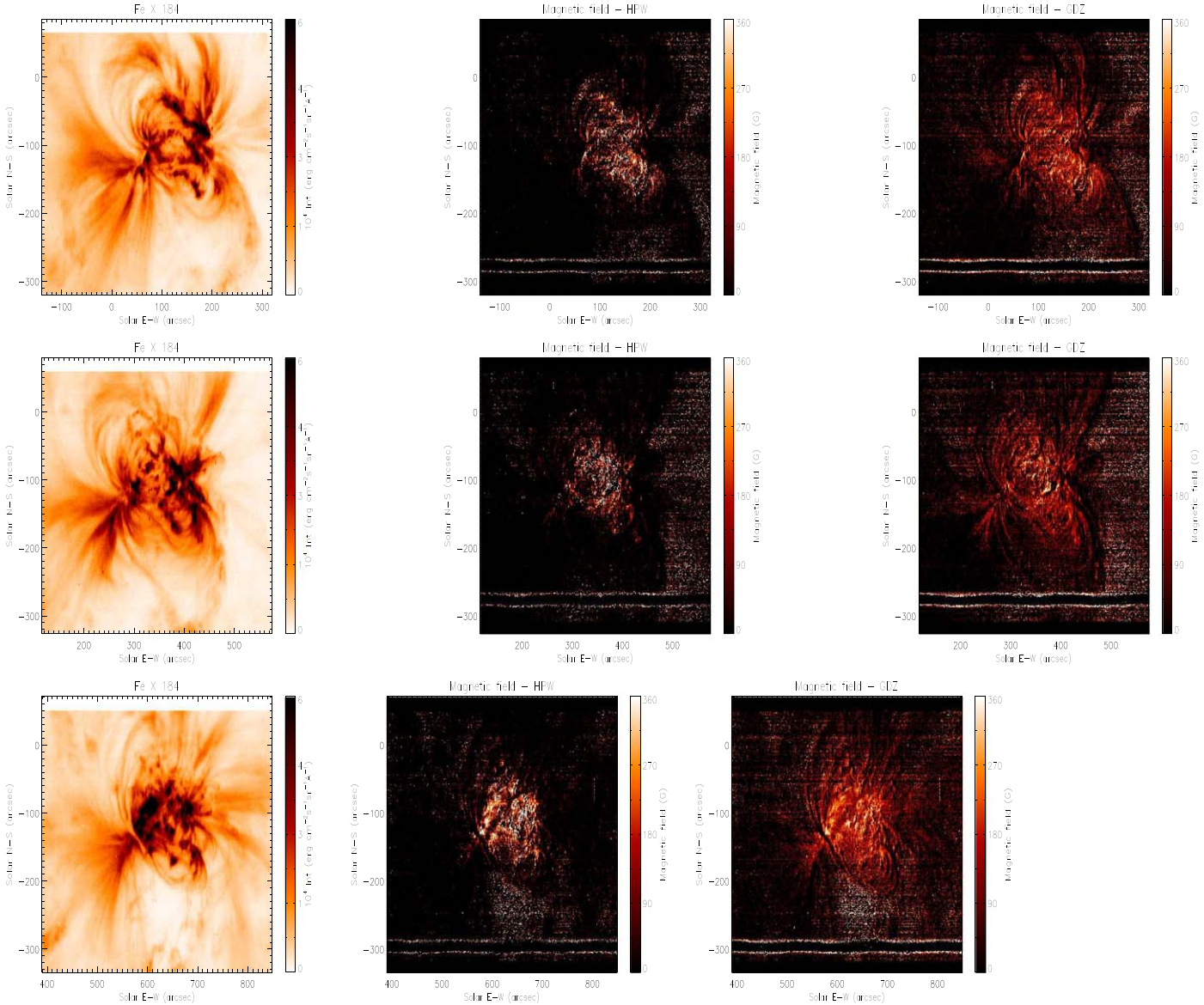

Figure 10. Comparison of magnetic field diagnostic results obtained with the HPW calibration (middle panels) and the GDZ calibration (right panels) from observations of AR10978.

image still has high quality, the S/N ratio has degraded significantly, and application of the diagnostic techniques, which need a high S/N, gives results plagued by both instrumental effects and significantly more noise than earlier in the mission. Results can still be reliably obtained (especially considering that no spatial rebinning or other correction was applied to the data sets shown in Figure 11), but the degradation of the instrument is apparent.

The effects of this degradation (included in the estimate of the relative intensity calibration provided in the previous section) have the additional consequence of lengthening the exposure time needed to reach a high-enough count rate in a single pixel to make Poisson noise negligible.

5.5. Atomic Data

The accuracy of the atomic data is also of critical importance for the present study. We have used CHIANTI version 9.0 to calculate line emissivities for all of the levels of Fe X and, when used for density diagnostics, Fe XI. The original sources for these data are del Zanna et al. (2010b) and del Zanna et al. (2013) for Fe XI and del Zanna et al. (2012) for Fe X. In both cases, large-scale models for the atomic target were considered. These works provided both energy levels: Einstein coefficients for spontaneous decay (A-values) and Maxwellian-averaged collision strengths.

The accuracy was benchmarked with observations from a number of laboratory, rocket, and space instrument measurements by del Zanna (2011), as well as by del Zanna et al. (2010b) and del Zanna et al. (2013) for Fe XI, by del Zanna et al. (2012) for Fe X, and more recently by Landi (2020, both ions). These studies, using many observations from a number of different instruments, found that the intensities of the spectral lines used in this work for magnetic field diagnostics were in excellent agreement with observations. Most importantly, most of the observations used to test Fe X were taken from quiescent spectra where the MIT transition is expected to be negligible, so the ambient magnetic field did not affect the results.

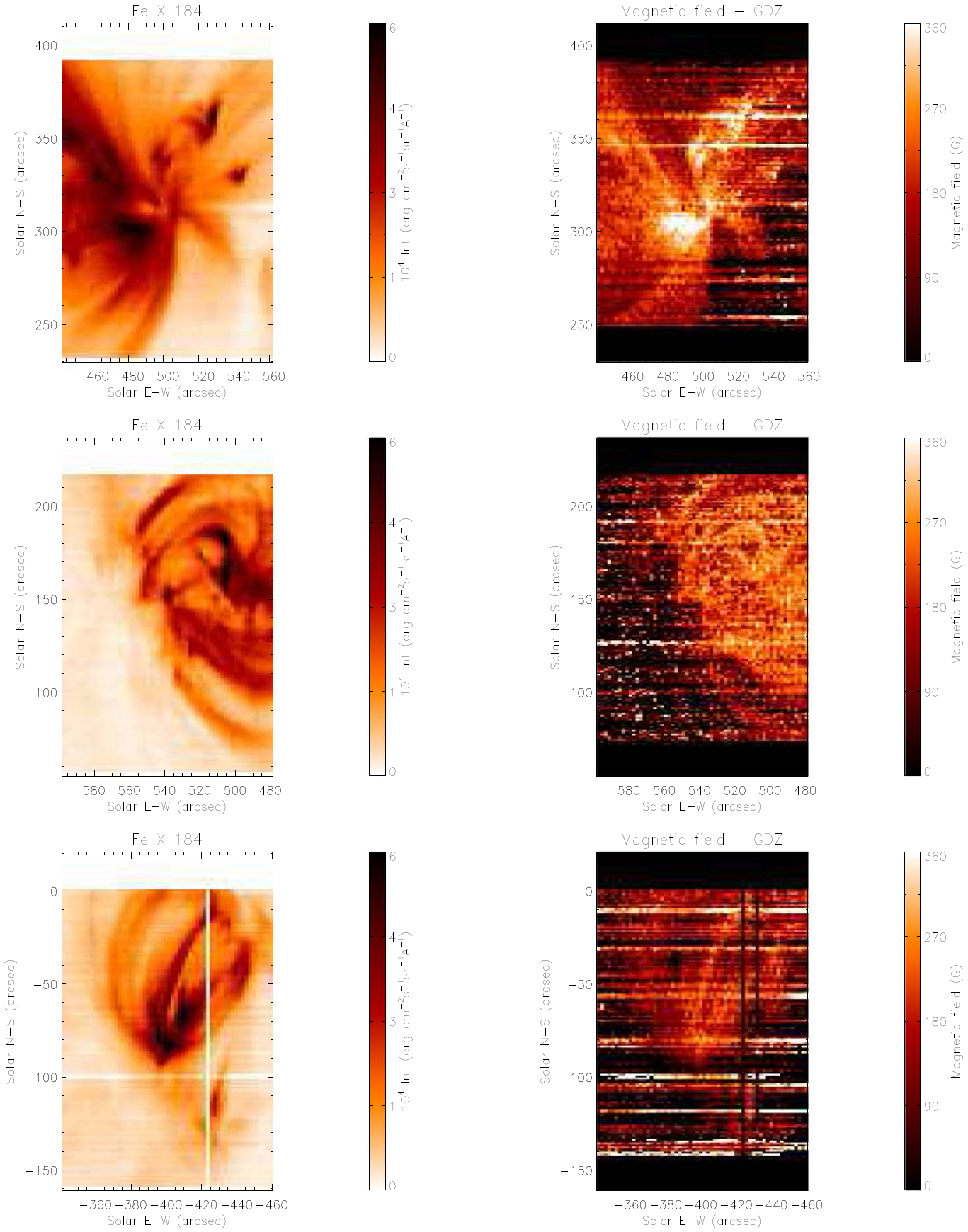

Figure 11. Effects of the degradation of the EIS sensitivity. Left panels: Fe X 184.54 Å intensity map; right panels: magnetic field measurements. Top: active-region observations taken on 2014 March 16 on AR12005; middle: active-region observations taken on 2016 October 25 on AR12603; bottom: active-region observations taken on 2018 December 28 on an unnumbered AR.

Still, any uncertainty in the atomic data will directly affect magnetic field measurements. In particular, at electron densities typical of active regions, both of the $^4D_{5/2,7/2}$ levels are populated mostly by radiative cascades from higher levels, so the accuracy of both collision excitation rates and Einstein coefficients involving levels different than $^4D_{5/2,7/2}$ is of great importance.

As an example, recently Wang et al. (2020) published a new, large-scale calculation for energy levels and A-values of Cl-like ions that also included data for Fe X. The much more extended model adopted in this calculation resulted in significant differences in the lifetimes and A-values of many of the levels in the $3s^2\ 3p^4\ 3d$ configuration; as the $^4D_{5/2,7/2}$ levels are mostly populated by cascades from $3s^2\ 3p^4\ 3d$ levels with higher energy, these differences can have significant effects on their level population and therefore their line intensities. In order to assess the relevance of this effect, we have repeated all of the measurements using an Fe X model that combined the Wang et al. (2020) Einstein coefficients with the CHIANTI 9 collisional data, finding that the measured magnetic field strengths increased by 20%–30% with this hybrid model over the values obtained utilizing the CHIANTI 9 data for both collisional and radiative data.

Unfortunately, Wang et al. (2020) only provided radiative data, lifetimes, and energy levels, but no collisional data, so a self-consistent calculation of line intensities could not be done. This comparison only underscores the need for new, large-scale calculations of Fe X collisional data using atomic models of the same accuracy as Wang et al. (2020). This is of course a formidable task, due to the added complexity in computing collision strengths, as well as other atomic properties involving continuum states, compared to rates in bound–bound transitions.

5.6. Uncertainty Estimate

The measurement of the magnetic field with the weak-field approximation is obtained from the $A_{\rm MIT}/A_{M2}$ branching ratio; combining Equations (3) and (6), we find the magnetic field can be rewritten as

$$B \propto \Delta E\ \sqrt{A_{M2}}\ \sqrt{\frac{I_{257}}{I_{184}} R\left[\frac{184}{M2}\right] - R\left[\frac{E1+M2}{M2}\right]} \qquad (7)$$

where $R(184/M2)$ and $R((E1+M2)/M2)$ are emissivity ratios. Thus, the final uncertainty in B is linearly proportional to the uncertainty of ΔE, while the square root decreases the effect of the uncertainties related to atomic physics, density diagnostics, and intensity calibration affecting the observed intensity ratio and the CHIANTI estimates of the emissivity ratios. A rigorous error propagation is difficult to make, because the errors due to density and atomic physics effects on the emissivity ratios are very difficult to combine; we can estimate that the final uncertainty of the magnetic field measurement, assuming the observed lines are sufficiently strong to make noise negligible, is around 70%, although a precise value is difficult to give.

In the strong-field technique, the magnetic field strength B cannot be cast explicitly as in Equation (7). Still, Equation (5) shows that the uncertainty is driven by the same factors as in the weak-field approximation: atomic physics (although only one CHIANTI ratio is now directly involved, somehow lowering the impact of this source of error), the determination of ΔE (which affects the value of $A_{\rm MIT}$ and thus the $^4D_{7/2}$ level population), and most importantly the EIS intensity calibration. The smaller sensitivity of this technique to B causes the calibration uncertainty to play a far more decisive role in limiting the measurements, making this technique of application difficult with the current status of the EIS calibration.

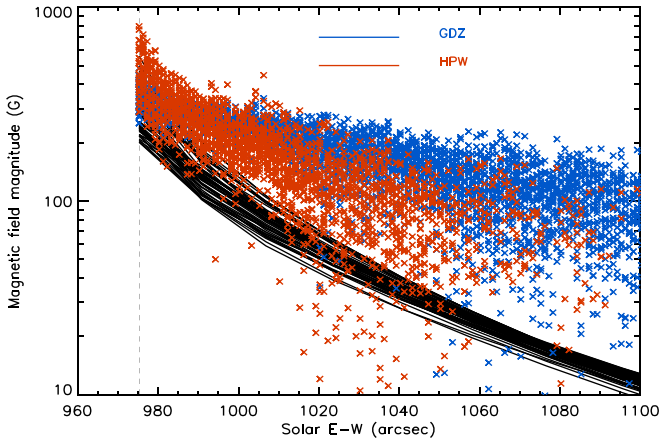

Figure 12. Comparison between the radial dependence of the magnetic field strength predicted by the PFSS model (black lines) on AR10978 with measurements obtained using the HPW calibration (red crosses) and the GDZ calibration (blue crosses).

The most important steps that need to be undertaken to improve the accuracy of this magnetic field technique are as follows:

1. Improve on SW/LW relative to the EIS calibration, and make sure that the intensity calibration of any new instrument that will observe these lines is very accurate.
2. Improve on the accuracy of the ΔE value, as its uncertainty directly affects the weak-field measurement.
3. Improve on the transition rates and collisional excitation rates necessary to calculate the emissivity ratios.

The first two items in the list are the most important uncertainty sources. Most notably, a definitive, more accurate determination of the LW/SW relative calibration (currently at the 50% level) will allow us to improve the estimate of the magnetic field in the strong-field approximation.

5.7. Comparison with Magnetic Field Extrapolations

Very few direct measurements of magnetic field strengths in active regions have been carried out, on different active regions than the ones that we studied. While the magnetic field strengths are similar to those we measure in the present work, a direct comparison is not possible.

We compared the present measurements with Potential Field Source Surface (PFSS) extrapolations (Schatten et al. 1969) of the magnetic field of the active region AR10978, focusing on the time (2007 December 18) when this region was observed at the limb. We used the PFSS package available in SolarSoft (Schrijver & DeRosa 2003). Since a direct, loop-by-loop comparison of the magnetic field is impossible, due to the difficulty of matching a single EIS structure with any particular PFSS field line, we compared the values of the magnetic field strength measured as a function of distance from the limb with the radial decrease of the PFSS magnetic field strength calculated over the active region. The active-region pixels were selected as those having a photospheric magnetic field larger than 200 G. The results are shown in Figure 12.

There are two things to notice. First, the magnetic field measurements reported in Figure 12 are overestimated when their values are larger than ≈200 G (see Section 4.2). While it is not easy to determine a correction to these measurements, we note that the field strengths measured at low heights are larger than but comparable to those predicted by the PFSS extrapolation, so the disagreement might be due to the limits of the weak-field approximation. It is expected that when the EIS calibration is determined to a much better accuracy, the strong-field technique will provide values in better agreement with the PFSS model.

Second, the rate of decrease with height of the measured field is slower than predicted by the PFSS model. This disagreement is expected, and it can be due to two causes. First, as the distance increases, the strength of the magnetic field and of the intensity of the other Fe X lines decreases, due to magnetic field and density fall-off, respectively. Thus, while at larger height the weak-field technique becomes applicable (and hence the measurement is more meaningful), the decreased S/N may make the measurement less reliable. Most importantly, active-region magnetic fields are nonpotential: potential fields fall off with height at a faster rate, due to their minimum energy state, than sheared, twisted fields (Mackay & Yeates 2012), so the predicted PFSS fields might be underestimated, with such underestimation increasing with distance.

It is worth noting that the HPW calibration provides fewer points at large altitude than the GDZ calibration. This is due to the former providing a lower 182.17/(188.22+188.30) intensity ratio than the latter, so at a large distance from the limb, where the electron density decreases below 10^7 cm^{-3}, the HPW calibration provides intensity ratios lower than the low-density limit, which are discarded by our software.

6. Discussion and Future Work

The present work illustrates the potential of a new diagnostic technique that allows the measurement of the magnetic field strength in active regions utilizing bright Fe X and Fe XI lines commonly observed by the Hinode/EIS satellite. This technique, which is based on a peculiar property found uniquely in two near-degenerate Fe X atomic levels, opens a new window on one of the most important and less measured quantities in solar physics: the coronal magnetic field.

The potential of this new diagnostic technique lies in two basic facts: (1) the coronal magnetic field determines all of the critical processes at the heart of coronal heating, plasma confinement, and the solar activity events (flares and coronal mass ejections) that give rise to space weather and to all of the adverse effects it has on human assets on the ground and in space; (2) this technique can be applied to any existing data set spanning from 2007 to 2020 (as of this writing), extending for more than one full solar cycle (including the anomalously weak minimum of solar cycle 24 in 2007–2009), and covering a large number of active regions, flares, and even coronal mass ejections. Thus, this new diagnostic technique opens the door for a whole new field of study.

The importance of this technique is all the more enhanced by the development and deployment of the next-generation ground-based observatories, which will be able to measure the coronal magnetic field orientation and line-of-sight component at the solar limb: DKIST and UCoMP. When combined at the limb, EIS, DKIST, and UCoMP observations will enable us to reconstruct the full magnetic field in coronal active regions, providing for the first time an observable of incalculable value for local and global models of active regions and of the solar corona. Furthermore, unlike UCoMP and DKIST, EIS can measure the coronal magnetic field on the disk, thus allowing the monitoring of active-region fields as they transit the disk: this capability enables the search for magnetic precursors to flares and coronal mass ejections, hopefully paving the way toward reliable space weather forecasting systems. Furthermore, this technique allows us to match magnetic field measurements to the determination of other properties that can be obtained with spectral lines from Fe X and other elements with the same instrument, providing a very complete characterization of active-region plasmas.

In this work, we present a few examples of the application of this technique to EIS observations taken at different times, monitoring the morphology, strength, and evolution of active-region magnetic fields. We find that the magnetic field strength in nonflaring active regions evolves both in morphology and strength over time, and its value ranges from a few tens to a few hundred gauss. The present technique is also able to provide 2D maps of the magnetic field in the plasma that emits Fe X line intensities.

Even more importantly, we present a list of EIS observing sequences whose data include all of the lines necessary for the application of this diagnostic technique, and a few more that include density-diagnostic line pairs from other ions that could also be used in some situations. We hope that this list will help the solar community navigate the immense set of EIS data and more easily find data to measure the coronal magnetic field strength.

However, this technique comes with limitations that need to be overcome. First and foremost, the calibration of the EIS instrument needs to be determined both as a function of wavelength and as a function of time across the entire EIS mission, so that uncertainties related to the relative calibration within and between the SW and LW detectors can be minimized as well. Intensity calibration uncertainty is at the moment the greatest obstacle to the application of this technique. The energy separation between the Fe X $^4D_{5/2,7/2}$ levels needs to be determined with even higher accuracy than obtained by Landi et al. (2020) so that the intrinsic uncertainty on the $A_{\rm MIT}$ value can be minimized. Also, we encourage the atomic physics community to improve on the radiative and collisional data for Fe X over what is currently available, in order to minimize the effects of errors in the atomic and collision parameters on the measured magnetic field strength.

E.L. was supported by NSF grants AGS 1408789 and 1460170 and NASA grants NNX16AH01G, NNX17AD37G, and 80NSSC18K0645. The authors would like to thank Dr. H.P. Warren for helpful discussions on the EIS intensity calibration and Dr. Chip Manchester and Mr. Yingjie Zhu for helpful suggestions on PFSS extrapolations and emissivity ratios. We would also like to thank the anonymous referee for her/his useful comments that helped improve the original manuscript.

ORCID iDs

R. Hutton https://orcid.org/0000-0001-6558-2820

References

Beiersdorfer, P., Scofield, J. H., & Osterheld, A. L. 2003, PhRvL, 90, 235003
Brosius, J. W., Landi, E., Cook, J. W., et al. 2002, ApJ, 574, 453
Brosius, J. W., & White, S. M. 2006, ApJL, 641, L69

Cranmer, S. R. 2009, LRSP, 6, 3
Culhane, J. L., Harra, L. K., James, A. M., et al. 2007, SoPh, 243, 19
Curdt, W., Landi, E., & Feldman, U. 2004, A&A, 427, 1045
de Moortel, I., Pascoe, D. J., Wright, A. N., & Hood, A. W. 2016, PPCF, 58, 014001
del Zanna, G. 2011, A&A, 514, A41
del Zanna, G. 2013, A&A, 555, A47
del Zanna, G., Andretta, V., Chamberlin, P. C., Woods, T. N., & Thompson, W. T. 2010a, A&A, 518, 49
del Zanna, G., Bromage, B. J. I., Landi, E., & Landini, M. 2001, A&A, 379, 708
del Zanna, G., & Mason, H. E. 2018, LRSP, 15, 5
del Zanna, G., Storey, P. J., Badnell, N. R., & Mason, H. E. 2012, A&A, 541, A90
del Zanna, G., Storey, P. J., & Mason, H. E. 2010b, A&A, 514, A40
Dere, K. P., del Zanna, G., Young, P. R., Landi, E., & Mason, H. E. 2019, ApJS, 241, 22
Dere, K. P., Landi, E., Mason, H. E., Monsignori Fossi, B. C., & Young, P. R. 1997, A&AS, 125, 149
Feldman, P., Levitt, M., Manson, S., & Novick, R. 1967, Phy, 33, 278
Gombosi, T. I., van der Holst, B., Manchester, W. B., IV, & Sokolov, I. V. 2018, LRSP, 15, 4
Judge, P. G., Hutton, R., Li, W., & Brage, T. 2016, ApJ, 833, 185
Kosugi, T., Matsuzaki, K., Sakao, T., et al. 2007, SoPh, 243, 3
Kramida, A., Ralchenko, Y., Reader, J. & the NIST ASD Team 2019, NIST Atomic Spectra Database (version 5.7.1), National Institute of Standards and Technology, Gaithersburg, MD, https://physics.nist.gov/asd
Landi, E. 2020, ApJ, submitted
Landi, E., del Zanna, G., Landini, M., et al. 1999, A&ASS, 135, 171
Landi, E., Hutton, R., Brage, T., & Li, W. 2020, ApJ, 902, 21
Landi, E., Landini, M., Pike, C. D., & Mason, H. E. 1997, SoPh, 175, 553
Lang, J., Kent, B., Paustian, W., et al. 2006, ApOpt, 45, 8689
Lemen, J. R., Title, A. M., Akin, D. J., et al. 2012, SoPh, 275, 17
Li, W., Grumer, J., Yang, Y., et al. 2015, ApJ, 807, 69
Li, W., Yang, Y., Tu, B., et al. 2016, ApJ, 826, 219
Mackay, D. H., & Yeates, A. R. 2012, LRSP, 9, 6
Nindos, A., White, S. M., Kundu, M. R., & Gary, D. E. 2000, ApJ, 533, 1053
Pesnell, W. D., Thompson, B. J., & Chamberlin, P. C. 2012, SoPh, 275, 3
Phillips, K. J. H., Feldman, U., & Landi, E. 2008, Ultraviolet and X-ray Spectroscopy of the Solar Atmosphere, Cambridge Astrophysics Series 44 (Cambridge, UK: Cambridge Univ. Press)
Schatten, K. H., Wilcox, J. M., & Ness, N. F. 1969, SoPh, 6, 442
Scherrer, P. H., Bogart, R. S., Bush, R. I., et al. 1995, SoPh, 162, 129
Scherrer, P. H., Schou, J., Bush, R. I., et al. 2012, SoPh, 275, 207
Schrijver, C. J., & DeRosa, M. L. 2003, SoPh, 212, 165
Si, R., Brage, T., Li, W., et al. 2020a, ApJL, 898, L34
Si, R., Li, W., Brage, T., & Hutton, R. 2020b, JPhB, 53, 095002
Stakhiv, M., Landi, E., Lepri, S. T., et al. 2015, ApJ, 801, 100
Stakhiv, M., Lepri, S. T., Landi, E., et al. 2016, ApJ, 829, 117
Suematsu, Y., Tsuneta, S., Ichimoto, K., et al. 2008, SoPh, 249, 197
Tomczyk, S., Card, G. L., Darnell, T., et al. 2008, SoPh, 247, 411
Wang, K., Jönsson, P., del Zanna, G., et al. 2020, ApJSS, 246, 1
Wang, T., Thomas, R. J., Brosius, J. W., et al. 2011, ApJS, 197, 32
Warren, H. P., Ugarte-Urra, I., & Landi, E. 2014, ApJS, 213, 11
Webb, D. F., & Howard, T. A. 2012, LRSP, 9, 3
White, S. M., Kundu, M. R., Garaimov, V. I., et al. 2002, ApJ, 576, 505
Wilhelm, K., Curdt, W., Marsch, E., et al. 1995, SoPh, 162, 189
Woods, T. N., Eparvier, F. G., Hock, R. H., et al. 2012, SoPh, 275, 115
Yang, Z., Bethge, C., Tian, H., et al. 2020, Sci, 369, 694
Young, P. R., Landi, E., & Thomas, R. J. 1998, A&A, 329, 291